Comparing the Urban Heat and Global Warming Impacts on Extreme Rainfall Characteristics in Pearl River Delta Based on Dynamical Downscaling

FUNG, Kwun Yip

A Thesis Submitted in Partial Fulfilment
of the Requirements for the Degree of
Master of Philosophy
in
Earth and Atmospheric Sciences

The Chinese University of Hong Kong
August 2018

Thesis Assessment Committee

Professor LEE Shing Yip (Chair)

Professor TAM Chi Yung Francis (Thesis Supervisor)

Professor TAI Pui Kuen Amos (Committee Member)

Professor LI Yubin (External Examiner)

Abstract

The Pearl River Delta (PRD), which located in Southeast China, is one of the global megalopolis undergoing rapid expansion since 1990s. In the past 60 years, a substantial increase (~ 5 – 10%) of the intensity of extreme rainfall over Southeast China has been observed; it is also projected to increase further in the 21st century according to the latest IPCC reports. Therefore, it is plausible that both global warming and urban effects are influencing precipitation characteristics over the highly urbanized Pearl River Delta megacity. This study examines the dual impacts of a warmer climate and anthropogenic heat released on heavy rainfall in PRD by using the Weather Research and Forecasting model coupled with a single-layer urban canopy to dynamically downscale GFDL-ESM2M simulations. Extreme rain events in south-eastern China, with intensities reaching the 99th percentile of daily precipitation are first identified in the GFDL-ESM2M present climate run and future (RCP 8.5) projections. These cases are then dynamically downscaled in two parallel experiments, one with zero anthropogenic heat (AH) flux (i.e. no anthropogenic heat effect), and another one with peak diurnal AH = 300Wm^{-2} (significant urbanization effect) in the urban area. Results show that, for non-TC related heavy rain events, the probability of extreme rain rate (> 10 mm hr^{-1}) in the urban domain are significantly enhanced when anthropogenic heat is incorporated. This is true in both the historical climate as well as the RCP 8.5 climate. Prescribed AH gives an increment of near-surface air temperature, leading to more Convective Available Potential Energy (CAPE) and less Convective Inhibition (CIN) in the urban domain. Hence, the atmosphere is more unstable, with stronger convection over the city and more intense rainfall over urban location. Comparing RCP 8.5 to the present-climate downscaling results, those based on the RCP 8.5 scenario show prominent warming signal within the whole troposphere. For the atmospheric environment during the extreme rainfall events, CAPE (CIN) is enhanced (reduced) in the whole PRD domain. The probability of extreme rain rate (> 20 mm hr^{-1}) is thus increased in both urban and non-urban regions for non-TC cases. Overall, it is seen that the anthropogenic heating can significantly enhance extreme rain of non-TC cases within the highly urbanized PRD region, with a magnitude that can be comparable to that due to global

warming. For TC-related cases, the responses to AH for historical and RCP 8.5 climate scenarios are different. Further analysis reveals that TCs do not consume local CAPE during the onset of heavy precipitation. The different convective processes associated with TC and non-TC related cases probably lead to their very different response of intense rainfall to AH imposed in a city.

摘要

自上世紀九十年代，位於中國東南部的珠三角洲的城市迅速擴張。近 60 年來，中國東南地區極端降水強度有增加約 5-10%，並預料於 21 世紀會繼續上升。珠三角上升的極端降水很大機會同時受全球暖化和城市化的影響。本研究運用了動力降尺度，將 GFDL-ESM2M 的模擬結果通過天氣模型結合單層城市冠層來動力降尺度，從而評估人為熱和全球暖化對珠三角極端降水的影響。在華南地區中，降水量在當前或 RCP 8.5 氣候情景達 99 百分位的極端事件被降尺為兩個實驗，一個無人為熱，另一個在城市地區有 300Wm^{-2} 人為熱。

人為熱都增加了兩個氣候情景“與颱風不相關”事件中城市地區降雨率 >10mm/hr 的概率。人為熱提升地面氣溫，增加了對流可用位能並減少了對流抑制能，令大氣變得不穩定，引致更強的降雨。至於全球暖化令到整個珠三角地區的對流層變暖，增強（減少）對流可用位能（對流抑制能），於是降雨率 >20mm/hr 的概率增加。總體而言，人為熱可以提高珠三角地區的“與颱風不相關”事件的強降雨率的幅度與全球暖化所導致的幅度相當。

人為熱對“與颱風相關”的事件在當前和 RCP8.5 氣候情景的影響不一致。分析顯示颱風的下雨機制不會利用當地的對流可用位能。“與颱風相關”和“與颱風不相關” 的對流機制不同，從而導致人為熱對兩者的影響不同。

Acknowledgement

I would first like to thank my thesis advisor Professor Tam Chi Yung Francis. Professor Tam inspired me throughout the study including the thinking process and the ways to present the work. The door to Professor Tam office was always open whenever I ran into a trouble or had a question about my research or writing. This work would not have been possible without the advice and support of Professor Tam. My sincere thanks also go to Dr. Wang Ziqian from the Sun Yat-Sen University. Without his participation in the method of dynamical downscaling, the whole project would not be a success. I would also like to acknowledge Professor Lee Shing Yip, Professor Tai Pui Kuen Amos, and Professor Li Yubin, as the readers of this thesis, and for giving me very valuable comments on this thesis. Finally, I must express my gratitude to my parents and to my friends for providing me with unlimited support and encouragement. This work would be impossible without them. Thank you.

List of Figures

Figure 2.6 Same as **Figure 2.5** except for nudging based on (a) winds, (b) geopotential height, (c) temperature, (d) winds and geopotential height, (e) winds, geopotential height and temperature and (f) winds, geopotential height, temperature and water vapour.

Figure 2.7 (a-c) Snap shot of rainrate during one selected extreme case from (a) GFDL-ESM2M historical run, (b) WRF-downscaled result without nudging and (c) WRF-downscaled results with U- and V-wind spectrally nudged from GFDL-ESM2M of wavelength ~ 1300 km. (d) Area-averaged rainrate over south China simulated by GFDL-ESM2M (black solid), WRF result without nudging (grey dotted), WRF result with nudged U- and V- wind of wavelength ~ 2000 km (green solid), ~ 1300 km (blue), ~ 1000 km (red solid) and ~ 800 km (orange solid).

Figure 3.1 Biases scatter plots for variables: (a) temperature (T_a), (b) geopotential height (H), (c) u-wind (U_a), (d) v-wind (V_a) and (e) precipitation (Pr) in MJJAS monthly climatology. For T_a, H, U_a and V_a, the plots are sub-plotted in (i) 1000 hPa, (ii) 850 hPa, (iii) 500 hPa and (iv) 200 hPa. Values computed in GFDL-ESM2M are plotted at y-coordinate and observations (ERA-Interim, TRMM-3B42) are plotted at x- coordinate. Blue lines are the regression lines for the scatter plots and red lines are the lines indicating ESM2M model result identical to observation. See text for details. Units of temperature: K, geopotential height: m, U- and V-wind: m s^{-1} and precipitation: mm day^{-1}.

Figure 3.2 Climatological seasonal mean (MJJAS) of (a) 500 hPa temperature, (b) 500 hPa geopotential height, (c) 850 hPa wind circulation overlaid on 850 hPa temperature and (d) daily precipitation amount at the (i) GFDL-ESM2M historical and (ii) observations (ERA-Interim for atmospheric variables or TRMM-3B42 for precipitation).

Figure 3.3 Taylor diagrams for (a) temperature (T_a), (b) geopotential height (H), (c) u-wind (U_a), (d) v-wind (V_a) and (e) precipitation (Pr) from GFDL-ESM2M, averaged over different seasons. Values are

List of Tables

Table of Contents

1. Introduction

Urbanization is defined as the process of human population clustering (Hope, 1942) which is associated with the change of natural into man-made land surface. Rapid urbanization has been observed over the past few decades in Pearl River Delta (PRD), the population grew from 40 million in 2000 to 120 million in 2011, and the urban area within has doubled in this period (Du et al., 2013). PRD is located in sub-tropical East Asia, which is strongly affected by the Asian monsoon. Heywood (1953) summarized that during summer several types of low-pressure systems can bring heavy rainfall to PRD and Hong Kong: (1) low-level troughs, (2) southerly or southwesterly wind due to the summer monsoon and (3) tropical cyclones. Heavy precipitation from these weather systems can lead to natural disasters such as flooding and landslides, thus posing great threats to thousands of people.

There are different elements from urbanization that affect the urban meteorology: (1) urban morphology (Oke, 1981; Kusaka et al., 2001; Coceal and Belcher, 2004; Shepherd, 2005), (2) urban land-surface properties (Bornstein, 1968; Carlson et al., 1981; Oke, 1988; Sisterson and Dirks, 2015) and (3) anthropogenic heat flux (AH) (Nielsen et al. 1981; Oke, 1988; Wilby et al., 2009). The effect of limited surface moisture availability at the urban area is well understood. However, the morphology and AH effect on rainfall are still not conclusive. AH effect was first selected to be further evaluated in this study. Most of the previous studies were based on single or a few extreme cases to study the AH effect, therefore the AH effect may not be significant. Furthermore, the effect of AH on extreme rainfall does not have a conclusive result yet; some studies found that AH enhanced rainfall, while some reported that rainfall was suppressed. Therefore, we used more than 20 extreme rainfall cases to examine the effect of AH on extreme precipitation over PRD.

Past studies about AH effect mostly depend on observations or simulations based on present climate, which may not applicable in the future warming world. Therefore, the other objective of this study is to evaluate the AH impact under global warming condition and to compare the global warming and AH effect. Understand the future AH effect on extreme rainfall is especially important for increasingly populated PRD region where casualties due to extreme rainfall related disasters are aboundant.

1.1. Urbanization in Pearl River Delta

Figure 1.1 compares the dominate land use classifications in 1993 with that over the year of 2002 in the PRD. It is clear that the area of urban land use has increased dramatically from 1990s to 2000's. Du et al. (2013) analysed different high resolution satellite imageries from the Land Satellite (Landsat) data in 1990, 2000 and 2010 and found that the fraction of urban area has constantly increased in this period. In 1990, built-up area contributed 3.56% to the total land area in PRD, while in 2010 the fraction was 15.18 %, comparable to figures from developed countries such as Belgium (20 %) and Germany (8 %) (Poelmans and Van Rompaey, 2009). The enlargement of urban area with an accelerated pace can be mainly attributed to the change of farmland into built up areas accompanying the fast economic growth in PRD (Du et al., 2013).

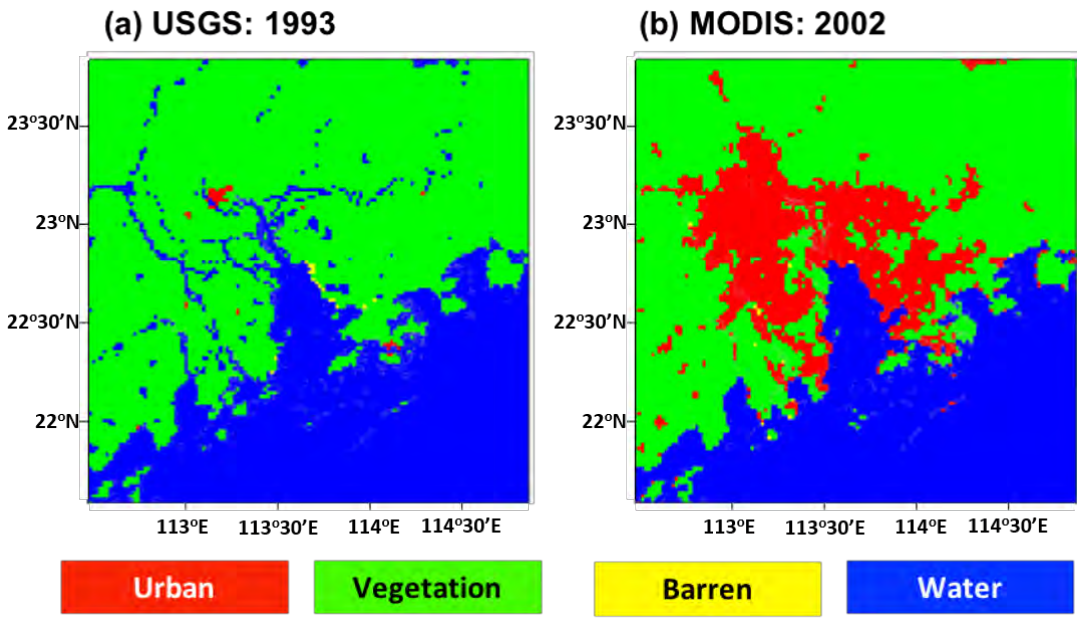

Figure 1.1 *Dominate land surface classification in (a) 2002 according to Moderate Resolution Imaging Spectroradiometer (MODIS) and in (b) 1993 according to United States Geological Survey (USGS). Four land use categories shown are: urban (red), vegetation (green), barren (yellow) and water (blue).*

1.2. Urban city-scale meteorology

Changing land surface from natural to man-made will lead to different interaction with the local atmosphere, especially at planetary boundary layer (PBL). In particular, an urban canopy layer (UCL), located at the lower part of PBL, can be formed inside the city area only (see **Figure 1.2**). Land surface properties, urban morphology, aerosols and anthropogenic heat (AH) are several major factors affecting the UCL moisture, energy and momentum budget. Shifting from vegetation into build up area will limit the surface moisture content, due to the impervious engineered surface. Hence, the evapotranspiration rate and moisture availability in the PBL are reduced. There is less moisture over the urban region compare with the rural area, especially during night-time in summer (Bornstein, 1968; Carlson et al., 1981; Oke, 1988; Sisterson and Dirks, 2015). Apart from the moisture content, changing the land surface properties will also reduce the energy budget due to reduction in latent heat flux (Bornstein, 1968; Oke, 1988; Sisterson and Dirks, 2015).

The roughness of a city is mainly governed by the city morphology, which characterized by building heights deviations, the distance between buildings etc. In spite of intensive studies over many years, it is still unclear how exactly urban morphology determines surface roughness. Coceal and Belcher (2004) found that increase in canopy density can decrease the mean wind speed, but the effect maybe reversed near ground surface for deep urban canopies. Buildings can also increase the surface roughness to trigger turbulence that can dynamically destabilizes the urban canopy layer (Shepherd, 2005) and provides extra lifting for air mass (Jin et al., 2015). Such turbulence might also induce convection and precipitation. Besides aerodynamic properties, radiative transfer is also affected by build-up features, which can be characterized by the aspect ratio of urban canyons and the sky view factor (defined as the percentage of visible sky in the overlaying hemisphere; Oke, 1981). Building walls and roof facets can trap and store heat during daytime and release it back in the nighttime. Radiation can also be trapped within the city due to multiple reflections (Arnfield, 2003; Kusaka et al., 2001; Kusaka and Kimura, 2004).

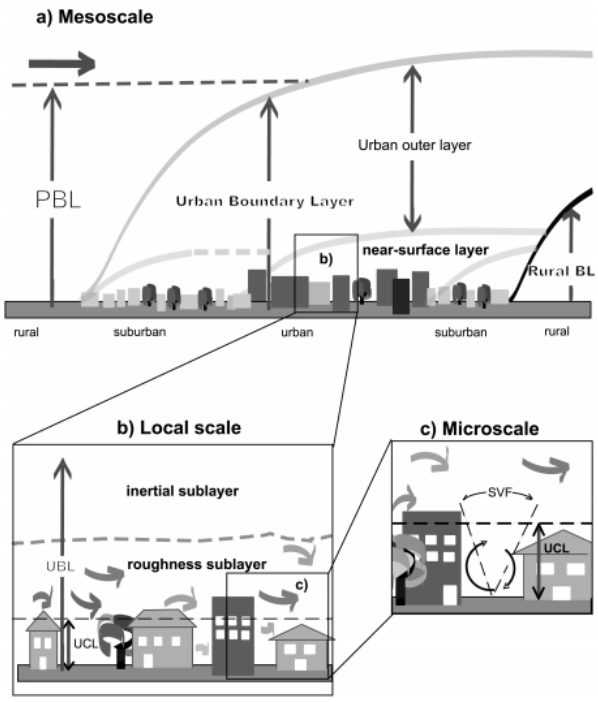

Figure 1.2 *Schematic diagram of the atmospheric flow and different scale lengths inside an urban city (a) at the meso-scale showing the urban boundary layer (UBL) and the rural boundary layer (RBL) and (b) the local scale with the UBL and urban canopy layer (UCL), (c) at the microscale within UCL. From Oke, (1976, 1988) and modified by Fisher et al., (2006).*

Urban aerosol is another factor affecting local meteorology especially precipitation. The aerosols mainly affect the rainstorm through the radiative budget and cloud microphysics. Air pollutants emitted by cars, factories can lead to a higher concentration of cloud condensation nuclei (CCN). More CCN can result in more cloud droplets but at the same time decreases the cloud droplets size, which in turn suppress precipitation efficiency (Collier, 2006; Jin et al., 2015). However, such an effect might be suppressed if the cloud top temperature is lower than normal (Jin et al., 2015). Rosenfeld et al., (2008) have another interpretation about the aerosol effect. Rosenfeld et al. proposed that aerosols can reflect solar radiation and suppress the evapotranspiration from the surface and reflected solar radiation, which stabilizes the troposphere and suppressed precipitation to occur. However, aerosols can serve as extra CCN which inhibit light rain and cloud can grow bigger before it starts raining. Therefore, the rainfall can be intensified by the aerosols.

Anthropogenic heat (AH) is the excess heat released from human activities. Sources mainly from buildings, vehicles, human metabolisms etc. (Allen et al., 2011). The value of AH cannot be directly measured but can be estimated based on surface energy balance (Oke, 1988; Wilby et al., 2009):

$$\text{AH } (\text{Wm}^{-2}) = Q^* - Q_H + Q_E + \Delta Q_S + \Delta Q_A$$

where Q^* is the net radiation received at the top of the city (i.e. difference between incoming and reflected short-wave radiation; Nielsen et al. 1981), Q_H is the sensible heat flux, Q_E is the latent heat flux (both calculated by satellite-derived surface temperature, wind speed, and moisture; Gaspar et al., 1990; Lei and Hanqing, 2017; Maltese et al., 2018), ΔQ_S is the heat storage and ΔQ_A is the heat advection.

The value of AH varies between different cities but typically ranges from tens to several hundreds W m^{-2}. The magnitude can even reach 1000 W m^{-2} at some very localized area such as central Tokyo (with values as high as 1590 W m^{-2} in winter; Ichinose et al., 1999), and Hung Hum district in Hong Kong (~ 1250 W m^{-2}; Oke, 1988). More recent studies show that the averaged AH value over Hong Kong urban area is ~ 300 W m^{-2} (Wong et al., 2015) and 120 W m^{-2} or more in Guangzhou (Yang et al., 2014).

AH typically has a diurnal cycle with either a single or double peak due to the habit of the residents within a city. On weekdays lots of people go to (get off from) work in the morning (evening), meaning that AH tends to have a double-peak diurnal profile. During weekends, people usually go out at noon, so that AH has a single peak profile (Allen et al., 2011; Xie et al., 2016).

1.2.1. Urban heat island (UHI)

The urban heat island (UHI) effect have been studied by meteorologists for decades (e.g. Nieuwolt, 1966). Studies showed that about 4 – 10 K temperature difference can exist between the rural area and urban core (Collier, 2006; Makar et al., 2006). The UHI profile is characterized by a hot core in the city center and slightly cooler at the surrounding (see **Figure 1.3**), and its magnitude is related to the population and lifestyle of citizens. Such temperature anomaly can affect the local circulation by modifying the pressure field, while changes in stability can also create turbulence (Collier, 2006; Jin et al., 2015). Studies also confirm that UHI can raise and destabilize the PBL (e.g. Makar et al., 2006). Under weak background wind conditions, UHI can generate circulation with updraft at the center of the city.

According to Lu et al. (1997), the height that hot air plume can reach is directly proportional to the Froude number ($F_r = U / (NL)$), where U is the background wind velocity and, N is the buoyancy frequency and L is the characteristics length of the UHI effect which is associated with the scale of city. The magnitude of the UHI is also directly related to the population of a city (Oke, 1973).

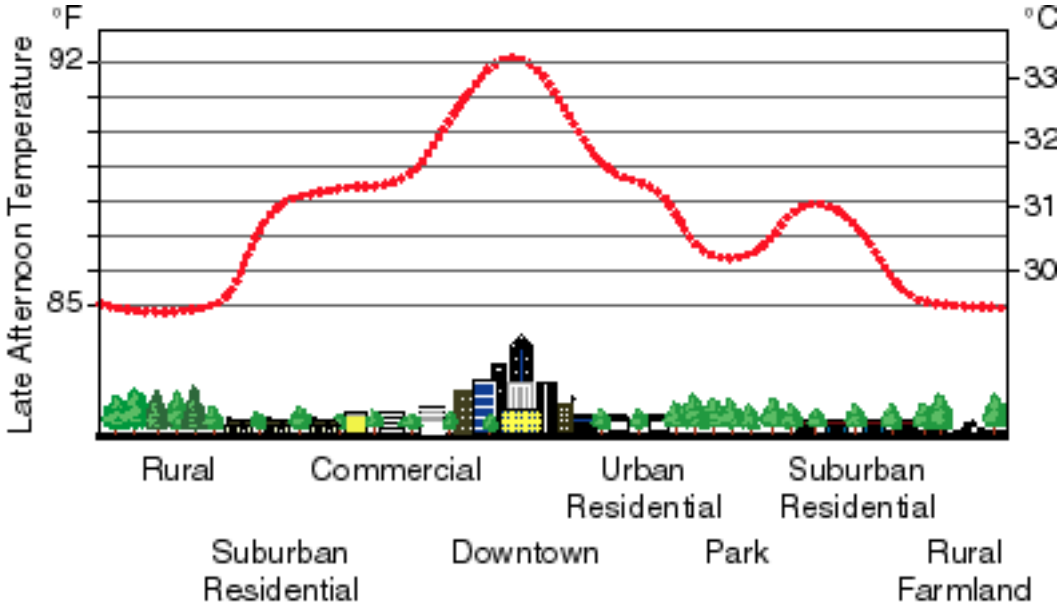

Figure 1.3 *Schematic diagram showing a general temperature profile over an urban area and its vicinity. From Onder and Dursun, (2010)*

1.2.2. Anthropogenic heat impacts on rainfall

The analysis of the relationships between anthropogenic heat and rainfall have been done in different locations and most of them focus on cities in the inland mid-latitudes. The Metropolitan Meteorological Experiment (METROMEX) from 1971 to 1975, focusing on inland mid-latitude cities including St. Louis, Chicago and Cleveland (Huff and Changnon, 1973) demonstrated that the total precipitation intensity can be enhanced at 10 – 80 km downwind of city centers. For coastal cities or megacities such as Tokyo (Kusaka et al., 2014), PRD (Holst et al., 2016), New Orleans, Houston and Washington (Huff and Changnon, 1973), results also show that total precipitation will be enhanced at the urban area or near the urban centers.

Bornstein and Lin, 2000 have examined six precipitation cases at Atlanta and found that the enhanced rainfall by UHI effect is observed over the urban and the downwind direction. They concluded that is due to the UHI-induced convergence. This result has been supported by other studies such as simulation experiment by Rozoff et al., (2003) over St. Louis.

There are also studies that show precipitation will be suppressed by UHI effect. Changnon and Karl, (2003) have examined rain events over Chicago, New York City and Washington. The results also show that UHI inhibits the precipitation. They concluded that these rain event occurred in the mid-latitude cities are freezing rain events. Therefore, the UHI effect prevents rain droplets from adhering on the cloud condensation nuclei surface, hence, precipitation is suppressed. Dou et al., (2015) have also investigasted the UHI effect in Beijing and find that for weak UHI effect which temperature is raised less than 1.25 K, the rainstorm may show splitting over the urban which suppress rainfall over urban.

From the results drawn by Dou et al., (2015), the strength of UHI is also an important factor that affects precipitation. The determinations of the magnitude of UHI have been introduced in section 1.2.1. Observations carried out during METROMEX suggest that for large cities (e.g. St. Louis, Chicago, Washington and Houston), precipitation intensity is enhanced over the urban as well as the downwind regions. However, in moderate-size cities (e.g. Indianapolis and Tulsa), urbanization has no significant effect on rainfall (Huff and Changnon, 1973).

The above studies are also focused on a few extreme cases study and Kusaka et al. (2014) made use of a high-resolution mesoscale model with urban physics incorporated to simulate the precipitation climatology over Tokyo. They showed that AH can enhance the climatological mean precipitation over the urban area. Although Kusaka examined the UHI effect based on long-term simulations, the rainfall cases coverage was from mild to extreme, meanging that the results might not be directly relevant to the impact of UHI on extreme rainfall.

To summarize the limitations in previous studies: (1) previous works on UHI effect mainly examine a few obseravations or simulated cases; (2) they mostly focus on mid-latitude cities, which have an atmospheric environment very different from the PRD; (3) they are based on observations or simulations for the present climate; (4) there is still no conclusive result on the UHI effect on extreme rainfall. Hence, it is important to carry out this study over the PRD area.

1.3. Impacts of global warming

1.3.1. Observation and simulation of global warming

The globally averaged carbon dioxide (CO_2) has increased from 340 ppm in 1980's to ~ 400 ppm in recent years, which in turn is the major contributor (80%) to global warming (IPCC, 2013). According to different datasets (Berkeley, CRUTEM, GHCN and GISS) the land-surface temperature has increased by ~ 1 K from 1980 to 2010, and the low troposphere temperature by ~ 0.3 K per in the same period.

To characterize the future emission and land use scenarios, the Representative Concentration Pathways (RCPs) are adopted (Moss et al., 2010). There are several RCPs commonly used, RCP 2.6, 4.5, 6.0 and 8.5. The number denotes the additional radiative forcing that the particular greenhouse gas emissions and concentration will give at the end of the century with the unit of Wm^{-2}. The RCP 8.5 scenario is considered to be the worst-case scenario that assumes no remediate measures will be take place to tackle global warming. At RCP 8.5 scenario, the CO_2 emission is assumed to be rising until the end of 21 century, with concentration > 1370 ppm without reaching a peak. This study has taken RCP 8.5 into considering in order to consider the the changes of extreme rainfall under the worst-case scenario.

1.3.2. Changes of mean precipitation under global warming

Under global warming, increased temperature will enhance the atmospheric moisture capacity and evapotranspiration, precipitable water is also increased. In the thermodynamic aspect, higher water content requires less vertical motion to create the same magnitude of rainfall. Therefore, the same convective system can create more intense rainfall in a warmer world. However, except for the atmospheric moisture availability, the atmospheric stability is also affected. More atmospheric moisture can enhance latent heat released at the upper troposphere, leading to a warmer upper atmosphere and creating a more stable atmosphere which in turn suppresses convection (Chou et al., 2012).

Global warming's impact on the monsoon circulations also leads to a spatially-varied response of the mean rainfall. In long-term, the ocean will heat up more compared to land. The differential heating weakens the thermal contrast between land and ocean (Ueda et al., 2006). Hence, the monsoon circulation is weakened,

which brings less moisture to land. However, observations show that East Asia Summer Monsoon (EASM) circulation does not have a significant trend in its strength in the past 50 years (Li et al., 2010), although a southward shift is noticed. Li et al. (2010) explained that this is due to the differential heating over the ocean which altered the monsoon circulation.

In summary, in spite of the increased moisture availability, due to the competing effects of atmospheric stability and change of circulation, the mean precipitation due to global warming is highly varied in different locations.

1.3.3. Changes of extreme precipitation under global warming

Global warming effects on extreme rainfall are mainly based on the Clausius-Clapeyron (CC) relationship. Increased temperature can raise the water capacity of air according to CC relationship (Ali and Mishra, 2017; Lenderink et al., 2011; Liu et al., 2015). From the relationship between the saturated vapour pressure (e_s) and temperature (T):

$$e_s(\text{hPa}) = 6.11 \times exp^{\frac{7.5 \times T(^{o}\text{C})}{273.3 + T(^{o}\text{C})}}$$

e_s increase by $\sim 6 - 7$ % per degree Celsius increased in near-surface temperature. Both water vapor capacity, and evapotranspiration rate increase can create a moister atmosphere. Extreme rainfall events tend to drain out moisture from the atmospheric column; therefore, the enhancement of atmospheric moisture can increase the extreme rainfall intensity.

Observations show that the response of rainfall toward global warming is different for different rain rates. Light rain intensity and frequency decrease, while heavy precipitation increases over different locations such as Hong Kong and Netherlands (Lenderink et al., 2011; Qian et al., 2007). Lenderink et al. (2011) showed that extreme rainfall intensity can increase in accordance with a super CC relationship (~ 14 % per degree K). According to the IPCC WG1 AR5 report, there is a significant increase for different rainfall extreme indices including R95p and SDII over south-eastern China for $\sim 5 - 10$ % in the past 60 years using HadEX2 with the latest version of European Climate Assessment dataset. The AR5 report also confirms that from both in-situ and satellite measurements, there is an increase in the frequency of heavy precipitation. Model projections also show that extreme rainfall in south-eastern China will further increase due to global warming.

1.3.4. Results from global circulation models

H. P. Chen, (2013) examined the future conditions under the RCP4.5 and RCP 8.5 scenarios with the 16 Coupled Model Intercomparison Project Phase 5 (CMIP5) models and found that heavy precipitation intensity (> 50 mm/day) will increase more than 32% in the late 21st century for both climates scenarios, while light rainfall (1 – 10 mm/day) would be suppressed. Chen concluded that the increment of precipitation is due to (1) the East Asian Summer monsoon which brings more moisture from the ocean to the land due to the enhanced atmospheric moisture and (2) the decreased the atmospheric stability leading to stronger convection. The shifting of rainfall PDF from light rain to heavy rain was also reported in different studies (Chou et al., 2012, Ueda et al., 2006). Model results are consistent with the present observation of extreme rainfall under the influence of global warming.

1.4. Downscaling techniques

Downscaling is a method to increase the spatial and temporal resolution of a coarse-resolution datasets or model products (Brown et al., 2008). The method is often applied to GCM outputs, so as to resolve fine-scale phenomena, and to incorporate local effects such as those topographic forcing and land-sea contrasts. Downscaling methods can be mainly divided into statistical downscaling and dynamical downscaling.

1.4.1.1. Statistical downscaling

The statistical downscaling method hinges on establishing an empirical relationship between large-scale circulation variables and the local weather conditions based on observational or historical data (Trzaska and Schnarr, 2014). There are various ways to carry out statistical downscaling, e.g. linear methods such as regression analyses and weather classification based on cluster analysis (Trzaska and Schnarr, 2014; Wilby et al., 2009). Compared to the dynamical downscaling methods (see below), statistical downscaling is relatively computationally inexpensive, easy to apply and can obtain down to station-scale information. However, this method is entirely empirical and may not capture the physical relationship between the local conditions and large-scale circulation. Moreover, the statistical relationships were built based on data in the past, which might require extrapolation to predict the future condition that lies beyond the current peak values.

1.4.1.2. Dynamical downscaling

In the dynamical downscaling method, a Regional Climate Model (RCM) is driven based on outputs from a coarse-resolution dataset such as reanalysis or GCM products. Initial, vertical and lateral boundary conditions are required from the coarse-resolution datasets to feed RCM in order to maintain the dynamical downscaling process (Trzaska and Schnarr, 2014). Both coarse-resolution datasets and RCM have to be carefully chosen, as their performance can affect the final downscaled products. RCM can incorporate more detailed physics, high-resolution topography and land surface characterization. Hence, by using the boundary conditions fed by coarse-resolution datasets, RCM can simulate higher-spatial (and temporal) resolution atmospheric conditions and resolve smaller scale weather systems. **Figure 1.4** gives a snapshot of precipitation rate before and after dynamical downscaling; the downscaled product can obviously capture much finer resolution

rainfall centers (see **Figure 1.4 b**) where cannot be seen in the original dataset (see **Figure 1.4 a**). An RCM has its own dynamical core, physics and values of parameters which may not be the same as the GCM; therefore, the downscaled results by RCM may not identical with those from the parent GCM. The greatest advantage of using dynamical downscaling is that it can capture the physics between atmospheric variables and the atmospheric processes explicitly. In this study, dynamical downscaling is used to carry out sensitivity tests about the impact of urban heating on local precipitation characteristics (see section **0**).

Statistical downscaling can relate different atmospheric variables together which may not have physical relationships but just coincident, the advantage of using dynamical downscaling is that the variables must be related with physical mechanisms which can be explained. Furthermore, statistical downscaling must be based on past occurred incidents, while dynamical downscaling is not constrained by the historical record, hence can be used for simulating the future climate scenario such as the RCP 8.5 scenario. Since dynamical downscaling does not require historical data to train the model, there is no limitation about experiments that can be done. In this study the effect of AH is tested by adding/removing AH flux from the urban area during the downscaling exercise, and to assess the impacts of global warming by dynamically downscaling present and RCP 8.5 climate scenarios.

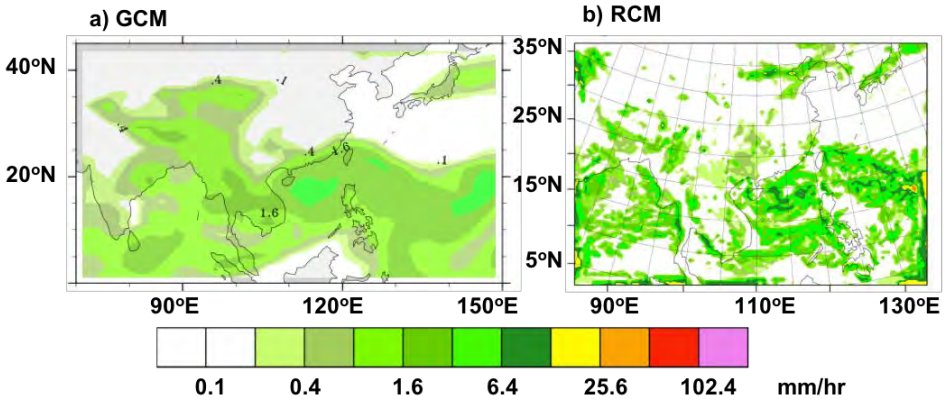

Figure 1.4 *Snap shot of precipitation rate (mm 3hr $^{-1}$) at the same time in (a) GFDL-ESM2M (GCM) and (b) WRF (RCM).*

2. Methodology

As mentioned in Chapter 1, previous studies focus on the UHI effect on urban focus on single cases of extreme rainfall. Kusaka et al. (2014) examined the climatological rainfall over Tokyo based on long-term integrations. There are also many studies that investigate extreme rainfall characteristic under the global warming background. However, thus far there is no study comparing the urban impacts and global warming influence on heavy precipitation over a city. This project seeks to address this issue with the following objectives: (1) to compare the change of rainfall characteristics under urban heating and global warming effects; (2) to understand the mechanisms of urban heating and global warming impacts on extreme rainfall; (3) to confirm the robustness of the UHI and global warming impact on heavy precipitation over PRD.

2.1. Outline of the study

In order to investigate the urban heating effect on extreme rainfall characteristics, a meso-scale model was used to dynamically downscale outputs from a GCM. Extreme cases were first identified in the GCM dataset and dynamical downscaling was carried out only for those selected cases using different experimental settings of urban parameters. This way, the effect of urban heating can be investigated. To investigate the global warming impacts, extreme cases were selected in GCM simulations for different climate scenarios. The GCM used in this study is GFDL-EM2M (see section 2.2), and the RCM used is the Weather Research and Forecasting (WRF) model with Advanced Research WRF (ARW) dynamic core version 3.8.1 (see section 2.4.1). To enhance the robustness the results, ~ 30 extreme rainfall events were first identified in GFDL-ESM2M historical (HIST) run and also the RCP 8.5 (RCP85) run individually. The extreme rainfall events were further inspected and stratified into those due to tropical cyclone (TC) occurrences and those not related to TCs (non-TC cases). All these cases were downscaled in two parallel sets of experimental settings, one with the diurnal maximum of AH = 0 W m^{-2}, and the other with AH = 300 W m^{-2} in the urban area. There are altogether 4 experiments (see **Table 2.1**) with different urban settings and climate backgrounds. The following section introduces the selection criteria of extreme rainfall cases in the GFDL-ESM2M datasets, and the way to carry out dynamical downscaling using WRF.

Experiments	*HIST_AH0*	*HIST_AH300*	*RCP85_AH0*	*RCP85_AH300*
GFDL-ESM2M scenarios	Historical		RCP 8.5	
Diurnal Maximum AH value (W m^{-2})	0	300	0	300

Table 2.1 *Experiments conducted in this study*

2.2. GFDL-ESM2M

The GCM we used in this study is Geophysical Fluid Dynamics Laboratory Earth System Model (GFDL-ESM2M) with Modular Ocean Model version 4 (MOM4) as ocean component developed by Geophysical Fluid Dynamics Laboratory (GFDL), National Oceanic and Atmospheric Administration (NOAA). GFDL-ESM2M and GFDL-ESM2G are the updated version of GFDL Climate Model version 2.1 (GFDL-CM2.1), and they share very similar physics. Both models have been selected in many climate projections studies within the group of CMIP5 models due to their satisfactory performance in many regions, such as South East Asia, Europe and Africa (e.g. McSweeney et al., 2015). There are only a few models perform well in simulating the climate in South East Asia and in particular the monsoon circulation, temperature, pressure annual cycle etc. The only difference between GFDL-ESM2M and GFDL-ESM2G is in their ocean component. The ocean model MOM4 that GFDL-ESM2M incorporates uses depth as the vertical coordinates, which gives better simulations in ocean ventilation, GFDL-ESM2G which uses density as vertical coordinates (Dunne et al., 2012, 2013). The atmospheric component of GFDL-ESM2M, which is the same as that of GFDL-CM2.1, has horizontal resolution of 2º x 2.5º in latitude and longitude. The new Land Model version 3.0 updates the hydrological cycle model physics and terrestrial ecology. GFDL-ESM2M was initialized with 1860 solar radiative forcing, present-day ocean temperature and present-day ocean salinity. For the atmospheric condition, results from the GFDL-CM2.1 1990 control run were used. This study used the historical and RCP 8.5 climate scenarios for downscaling. 60 years were taken from the historical run, from 1946 to 2005, and 95 years from the RCP 8.5 scenario from 2006 to 2100.

2.3. Case Selection

This section introduces the method of identifying extreme rainfall cases in South China from the GFDL-ESM2M historical run and future climate projections based on the RCP 8.5 scenario. These GCM-simulated heavy rainfall events will be further downscaled by WRF, focusing on the PRD region.

2.3.1. Extreme cases selection

The daily rain rates from the GFDL-ESM2M simulations are used to identified extreme rainfall cases. In particularly, daily mean precipitation in the region of 17 – 27 ºN, 105 – 117 ºE (see **Figure 2.1**) for both historical and RCP 8.5 runs were first computed. This region was selected based on 16 grids in the GFDL-ESM2M over the PRD region. The PRD only occupied one grid in GFDL-ESM2M; however, to avoid any bias selection due to the location selection, we expand region of interest to 16 grids. Based on the resulting probability for wet days (> 0.1 mm day^{-1}), days during which exceeds the 99^{th} percentile (R99p) were considered as "extreme precipitation days". "Extreme cases" were then found by clustering consecutive extreme precipitation days. 110 and 180 cases were found in historical and RCP 8.5 runs respectively. About 75 % of extreme rainfall cases identified this way occurred within the extended summer of May to September for both climate scenarios. This is consistent with the understanding that major contributors to extreme rainfall in this region, such as tropical cyclones, low-level troughs and other low-pressure systems, tend to occur in summer. Therefore, only summertime extreme events were investigated in this study.

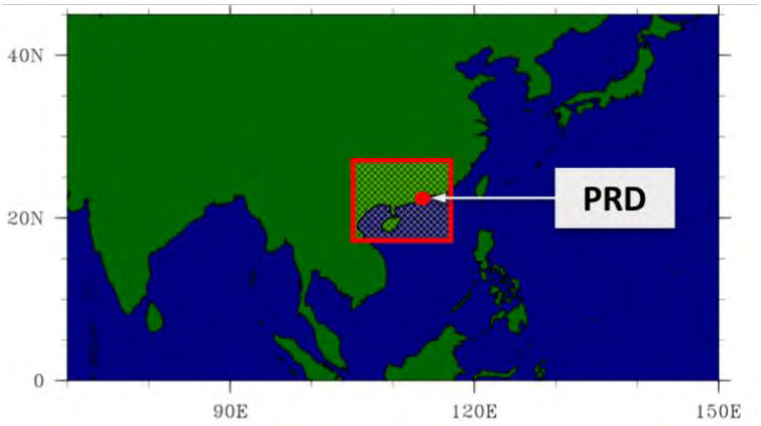

Figure 2.1 *The 17 – 27 ºN, 105 – 117 ºE region in south-eastern China for identifying extreme rainfall cases. The red dot denotes the location of PRD.*

Downscaling all 290 cases for both climate runs using a 3-domain nesting would be extremely computational expensive. Therefore, only ~ 60 cases in each climate senario were first randomly selected in this pool of identified cases in each climate scenario and downscaled with a 1-domain setting, using the outermost domain (see section 2.4.2.1). Outcomes from these ~ 120 cases were further examined, and only those that can capture the rain rate peak with an offset of at most $\pm$ 24 hours compared with GFDL-ESM2M simulations were selected. These chosen cases were then separated into TC induced cases and non-TC related cases by inspection; cases that TC rain band strike PRD were defined as TC induced cases, otherwise they belong to non-TC induced cases (see **Table 2.2** for the numbers of downscaled TC and non-TC events). These cases were then further downscaled using a 3-domain one-way nesting to 2-km resolution (see section 2.4.2).

	Historical	**RCP 8.5**
Number of cases simulated	39	44
TC cases	13	17
non-TC cases	26	27

Table 2.2 *Numbers of TC and non-TC related extreme rainfall cases selected for dynamical downscaling to 2-km resolution.*

2.4. Dynamical downscaling of extreme rainfall cases

After identifying extreme rainfall cases in GFDL-ESM2M, dynamically downscaling using the Weather Research and Forecasting model (WRF) coupled with a single-layer urban canopy model (SLUCM) were applied. Before going into the details of dynamical downscaling, the WRF model is first introduced.

2.4.1. The Weather Research and Forecasting (WRF) model

The WRF model with Advanced Research WRF (ARW) dynamic core version 3.8.1 is a non-hydrostatic model developed collaboratively by the National Center for Atmospheric Research (NCAR) of National Centers for Environmental Prediction (NCEP) National Oceanic and Atmospheric Administration (NOAA) and other laboratories. WRF is often considered as the state-of-art model and with large flexibility, and it provides a broad range of options for different physical processes. It is maintained as a community model and widely used in both weather forecasting and regional climate studies. Users around the world can feedback and improve the source code; hence, WRF constantly undergoes updates (Skamarock et al., 2008).

2.4.2. WRF model setup

2.4.2.1. Model domain

In this study, the meso-scale model WRF was integrated with 3 nested domain, using one-way nesting (see **Figure 2.2 a** for domain configuration). Geographical domains were chosen based on the following considerations (1) to avoid cross-cutting steep relieve, which prevents reflected signals entering the inner domains and give incorrect results (see **Figure 2.3** for topography in each domain); (2) to keep the region of interest at the centre of the innermost domain and away from the influence of boundaries. In each domain, the relaxation zone has a width of 4 grids boxes and results in these zones were not considered in the results. WRF was integrated with horizontal spatial resolution of 50 km x 50 km in the outermost domain (d01), with 129 x 89 grids in zonal and meridional direction respectively in time steps of 90 s. The middle domain (d02) was integrated with lateral spatial resolution of 10 km x 10 km, with 70 x 80 grids and in time steps of 18 s. The innermost domain (d03) has the resolution of 2 km x 2 km, giving 130 x 130 grids with integration time steps of 3.5 s. See **Table 3.3** for the detailed model configuration.

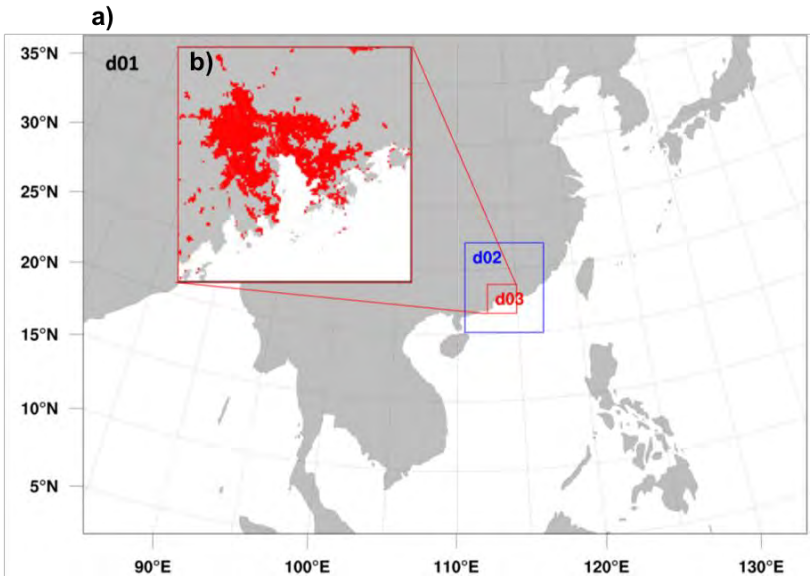

Figure 2.2 *(a) Domain coverage in WRF for all experiments. (b) Urban land use is shown in red in d03.*

In WRF several different land use datasets are available. Two of the most well documented are the USGS in 1993 and MODIS in 2002 datasets (see **Figure 1.1**). The MODIS dataset contains 21 land use categories including 13 types of vegetation, 2 types of water bodies, 3 types of tundra, snow, barren land and urban. When coupled with SLUCM, the urban land category can be further divided into low-density residential, high-intensity residential and commercial. However, due to the limited data at hand, all urban grid points were regarded as high-intensity residential for simplicity, giving albedo of 0.15 and surface emissivity of 0.88 in both summer and winter seasons. **Figure 2.2 b** shows the urban area in d03 (shading) according to the MODIS data.

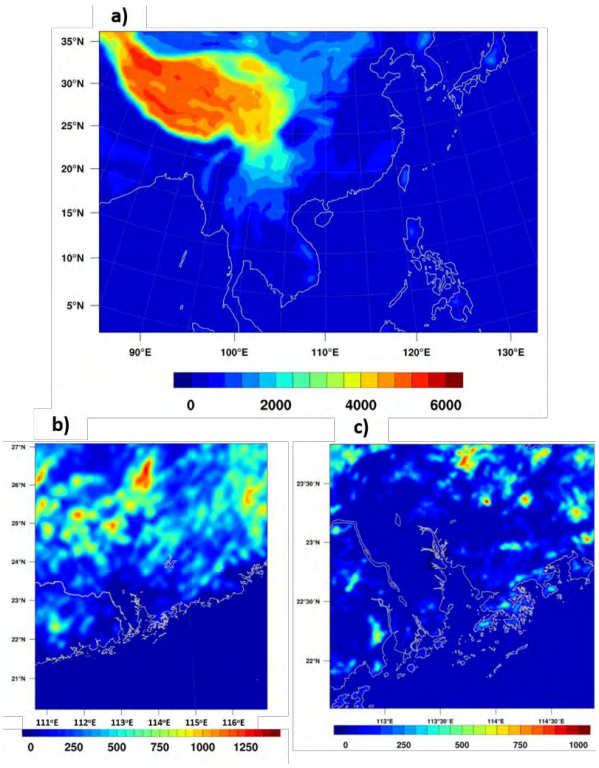

Figure 2.3 *Topography in (a) d01, (b) d02 and (3) d03.Units: m*

2.4.2.2. Model Physics

Physical parameterization adopted in our WRF experiments include the Rapid Radiative Transfer Model for GCMs (RRTMG), long-wave radiation scheme by Iacono et al. (2008), Dudhia short-wave radiation scheme (Dudhia, 1989), the single-moment 6-class microphysics scheme (Hong and J. Lim, 2006), the Eta similarity theory (Janjić, 1994; Monin and Obukhov, 1954) for surface layer option, Simplified Arakawa-Schubert (SAS) cumulus scheme (Pan and Wu, 1995) and Bougeault – Lacarrere planetary boundary layer (BouLac PBL) scheme (Bougeault and Lacarrere, 1989). For detailed description of the model setting, see also the study by Holst et al. (2016). Cumulus parameterization was only used for the outermost domain. This also reduces the discontinuity between simulations in d02 and d03. According to WRF tutorial (https://dtcenter.org/events/wrf-nmm_tutorial06_summer/Presentations/NMM_Physics_Dudhia.pdf), Mellor-Yamada-Janjic (Eta/NMM) is a better choice for the boundary layer option when using Monin-Obukhov similarity theory as surface layer option. However, in this model configuration, Mellor-Yamada-Janjic produced unstable solutions in some extreme rainfall cases. Various boundary layer options have been tested and only BouLac PBL gave stable solutions. **Table 2.3** summarizes the physical parameterization schemes used.

	d01	d02	d03
Start time	Case dependent (72 hours before and after the peak for most cases)		
End time			
Time interval (s)	90	18	3.5
Domain coverage (lat, lon)	2.23° – 43.82°, 70.81° – 147.05°	19.94° – 27.09°, 110.68° – 117.60°	21.50° – 23.83°, 112.51° – 115.04°
Vertical layers	27 layers		
Soil layers	4 layers		
Longwave radiation	RRTMG		
Shortwave radiation	Dudhia		
Microphysics	WSM 6-class		
Surface layer	Monin-Obukhov similarity theory		
Boundary layer	BouLac PBL		
Cumulus parameterization	Simplified Arakawa-Schubert (SAS) GFS scheme		Off
Urban Canopy Model	Bulk parameterization		SLUCM

Table 2.3 *WRF model configurations in d01, d02 and d03*

2.4.2.1. Urban canopy model in WRF

WRF also has options for coupling with an urban canopy layer which can simulate micro-scale meteorology within and above the city. There are three methods to simulate the urban effects on local meteorology: (1) bulk urban parameterization, (2) single-layer urban canopy model and (3) multi-layer urban canopy (BEP) and indoor-outdoor exchange model (BEM). For all these options, the NOAH land surface model has to be adopted in the setting of WRF.

In bulk parameterization, vegetated fraction and evapotranspiration for an urban grid is reduced, while roughness length set to the value of 0.8 m (F.Chen et al., 2011), which is a rough estimation for urban environment. In comparison, the single-layer urban canopy model (SLUCM) is more comprehensive (Kusaka and Kimura, 2004). Urban land use is further divided into low-density residential, high-density residential and commercial land use. SLUCM also incorporates information about urban geometry by considering building height, road width and roof width to represent the shadowing effect and reflection of radiation within the city. SLUCM also allow users to provide values of anthropogenic heat (AH), the roughness length, etc. Altogether, around 20 parameters (see **Table 2.4**) are needed to quantify the physical properties of the city.

Within the urban area, roads, building walls and roof tops can absorb and reflect radiation, which traps radiation inside the urban city. Direct and reflected radiations are also included in SLUCM to mimic this effect. The sensible heat flux is calculated by Jurges formula using the temperature difference between (1) building wall surface and the atmosphere and (2) roads and the atmosphere (Kusaka and Kimura, 2004). Momentum and energy exchange between the urban canopy and the free atmosphere are computed based on Monin-Obukhov similarity theory.

Parameter	Unit	SLUCM	BEP-BEM
Building height	m	Yes	Yes[#]
Standard Deviation of roof height	m	Yes	No[#]
Roof width	m	Yes	Yes[#]
Road width	m	Yes	Yes[#]
Anthropogenic heat	$W\ m^{-2}$	Yes	No
Anthropogenic heating diurnal profile	Fraction	Yes	No
Fraction of the urban	Fraction	Yes	Yes
Heat capacity of roof	$J\ m^{-3}\ K^{-1}$	Yes	Yes
Heat capacity of building wall	$J\ m^{-3}\ K^{-1}$	Yes	Yes
Heat capacity of road	$J\ m^{-3}\ K^{-1}$	Yes	Yes
Thermal conductivity of roof	$J\ m^{-1}\ s^{-1}\ K^{-1}$	Yes	Yes
Thermal conductivity of building wall	$J\ m^{-1}\ s^{-1}\ K^{-1}$	Yes	Yes
Thermal conductivity of road	$J\ m^{-1}\ s^{-1}\ K^{-1}$	Yes	Yes
Surface albedo of roof	Fraction	Yes	Yes
Surface albedo of building wall	Fraction	Yes	Yes
Surface albedo of road	Fraction	Yes	Yes
Surface emissivity of roof	-	Yes	Yes
Surface emissivity of building wall	-	Yes	Yes
Surface emissivity of road	-	Yes	Yes
Roof momentum roughness length	m	No	Yes
Building wall momentum roughness length	m	Yes*	No
Road momentum roughness length	m	Yes*	Yes*

Table 2.4 *Parameters required in SLUCM and BEP-BEM*

* Only used such parameter if Monin-Obukhov similarity theory options is selected

[#] Urban morphology specified by distribution table

2.4.2.2. SLUCM set up

SLUCM instead of the multi-layer UCM (BEP-BEM) was used here. This is because BEP-BEM requires very detailed information on building height density. For simplicity, SLUCM was used a mean building height of 30 m (from the Hong Kong Lands Department). For the standard deviation of building height, the defaulted commercial land use value was adopted which was 4 m. The road width was set to 16.0 m, the estimation based on the values of street canyon aspect ratio ranging from 1:3 (in Sham Shui Po) to 1:7 (in Causeway Bay) in Hong Kong (Chan and Kwok, 2000). The choice is consistent with the Hong Kong Planning Standards and Guidelines (https://www.pland.gov.hk/pland_en/tech_doc/hkpsg/full/ch8/pdf/ch8.pdf).

Peak AH fluxes over urban area in both summer and winter averaged over Hong Kong urban area retrieved from satellite measurements were estimated to be 289.16 W m^{-2} and 283.17 W m^{-2}, respectively. In some densely populated regions such as Mong Kok, it can even be as high as 1000 W m^{-2} (Wong et al., 2015). Such high value matches with the in-situ measurements done in Hung Hom in 1988 (Oke, 1988); in the same district the annual mean AH flux was 350 W m^{-2}, comparable with highly urbanized cases in Tokyo (400 W m^{-2}) (Ichinose et al., 1999) and New York (150 W m^{-2}) (Taha, 1997). Here the peak AH flux was set to 300 W m^{-2} within the 24-hour cycle. The AH value had a double-peak diurnal profile with maxima at 7 a.m. and 4 p.m. local time. The averaged AH flux was 166 W m^{-2} and minimum AH flux was 21 W m^{-2} at 3 a.m. local time (see **Figure 2.4**).

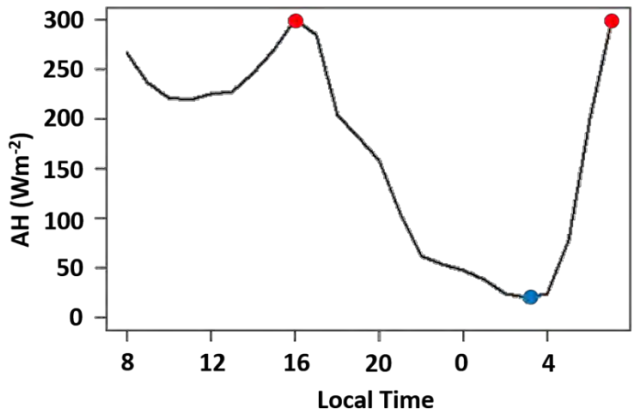

Figure 2.4 *Diurnal profile of AH prescribed over urban grids in d03 for experiments with peak AH = 300 W m^{-2}. Maximum AH occurs at 7 a.m. and 4p.m. local time. The daily averaged AH value is 166 W m^{-2}.*

2.4.2.3. Dynamical downscaling and spectral nudging

For dynamical downscaling, wind, specific humidity, air temperature, near-surface wind, near-surface specific humidity and near-surface temperature were taken from GFDL-ESM2M outputs every 6 hours. Daily mean sea surface temperature, as well as monthly mean soil water content, soil temperature, and surface temperature were also adopted in WRF to avoid the inconsistent land surface condition between WRF initialization and GFDL-ESM2M conditions. To increase the consistency between GFDL-ESM2M and WRF spectral nudging was also imposed.

Spectral nudging is a commonly used method to impose the synoptic circulation features in GCMs to the RCM environment (von Storch et al., 2000). Nudging variables in WRF include winds, geopotential height, temperature and water vapour at various wavelengths, nudging levels and strengths. One extreme event in GFDL-ESM2M was selected to evaluate the best configuration by comparing the rainfall intensity at south-eastern China (17^{o} – 27 ^{o}N, 105 – 117 ^{o}E) from GFDL-ESM2M and that in WRF.

According to Lo et al. (2008), nudging should be applied based on the principle of maximize degree of freedom for WRF. Hence, the nudging level should be high enough such that the lower troposphere including the Planetary Boundary Layer (PBL) can evolve according to WRF's internal dynamics. The extreme event was downscaled with wind, geopotential height, temperature and water vapour nudged into two experiments, nudged the variable (1) in the whole atmospheric column expect the PBL and (2) above 500 hPa only (see **Figure 2.5**). It was found that the choice of the nudging level did not affect the overall results; nonetheless nudging level above 500 hPa was adopted.

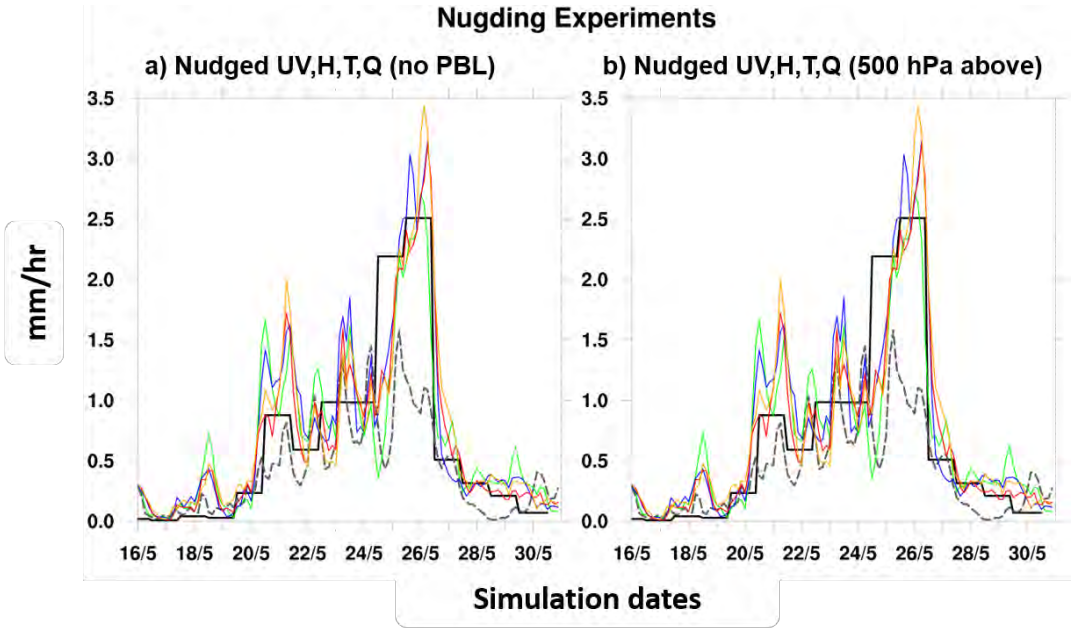

Figure 2.5 *Rainfall with wind, geopotential height, temperature and water vapour nudged over the (a) whole atmospheric column except PBL and (b) above 500 hPa at different wavelengths and above: ~ 800 km (orange), ~ 1000 km (red), ~ 1300 km (blue), ~ 2000 km (green). The black dotted line indicates the WRF results without any nudging and black solid line indicates results from GFDL-ESM2M.*

Different combinations of variables for nudging and the choice of wavelengths were evaluated. From **Figure 2.6**, the rainfall from WRF without using spectral nudging (black dotted line) cannot capture the intensity of the peak rainfall in south-eastern China in GFDL-ESM2M (black solid line). All experiments in **Figure 2.6 a** can capture the rainfall peak at 25th May, and the choice of wavelengths only slightly alters the rainfall intensity. From the results in **Figure 2.6 a** and **Figure 2.6 d** (nudged both wind and geopotential height), it can be concluded perturbing geopotential height does not have any effect on rainfall intensity. This result was validated with **Figure 2.6 b** (nudged geopotential height alone). From **Figure 2.6 c**, nudging with wavelength less than 1300 km for temperature can reproduce the peak of rainfall at 25th May. However, for nudging wavelength ~ 2000 km, rainfall was overestimated. Hence, nudging temperature alone is not a suitable choice. **Figure 2.6 e**, shows that nudging temperature with wind and geopotential height can reproduce the rainfall time series pattern by suppressing the overestimation peak at 20th May. By comparing **Figure 2.6 e and f**, nudging water vapor also does not affect the rainfall intensity.

To allow the maximum degrees of freedom in the system, only synoptic or larger scale circulation should be nudged, i.e. features with wavelengths > 1000 km, so as to leave the meso-scale meteorology to evolve dynamically in WRF. From these experiments, it can be concluded that nudging multiple variables does not enhance the accuracy of timing and intensity of the rainfall event substantially. Therefore, the strategy of nudging wind alone at the wavelength ~ 1300 km or above was adopted.

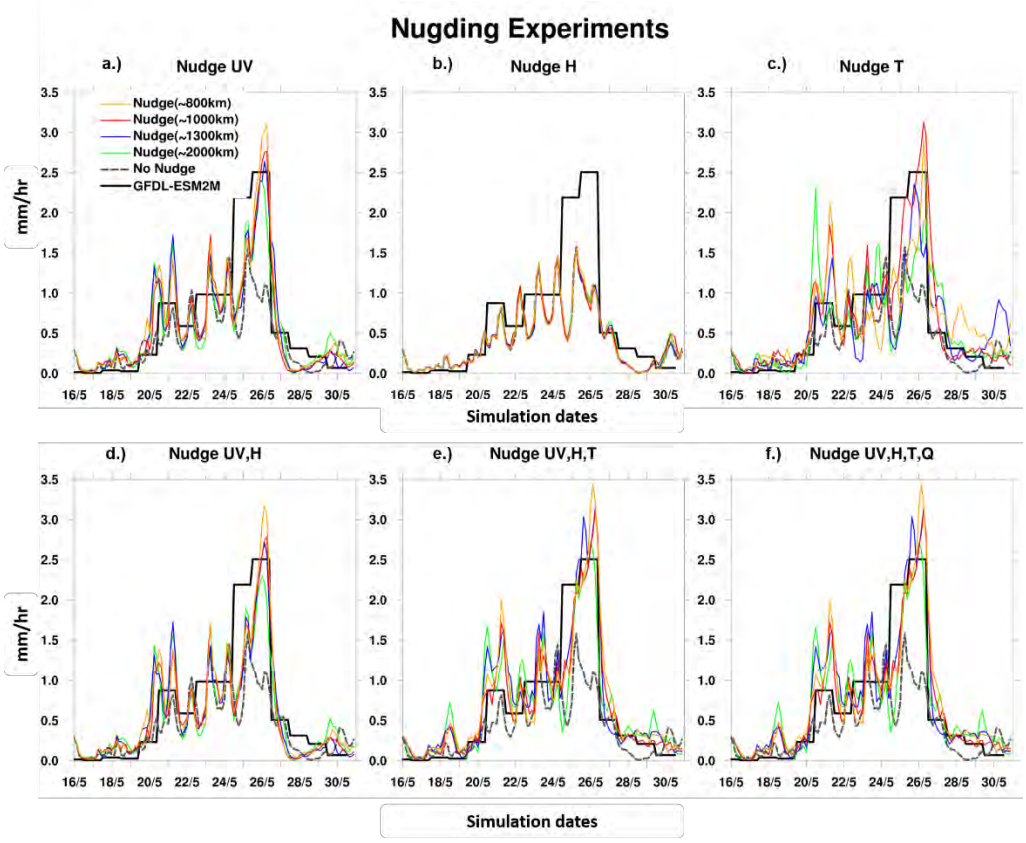

Figure 2.6 *Same as* ***Figure 2.5*** *except for nudging based on (a) winds, (b) geopotential height, (c) temperature, (d) winds and geopotential height, (e) winds, geopotential height and temperature and (f) winds, geopotential height, temperature and water vapour.*

Typical nudging coefficient representing the nudging strength for wind, temperature and water vapour at the 36 km resolution is 3 x 10^{-4} s^{-1} (Otte and Gilliam, 2007). In this study, spectral nudging was only applied in the outermost domain (d01) with 50 km resolution. Therefore, the value of 3 x 10^{-4} s^{-1} was considered to be reasonable. **Figure 2.7** compares results before and after applying spectral nudging. From the GFDL-ESM2M dataset, there is a strong rain centre over PRD (see **Figure 2.7 a**). It is seen that the rainfall pattern cannot be captured without nudging, leading to an underestimation of rainfall intensity (see **Figure 2.7 d**). Strong rain over the

PRD region can be captured when spectral nudging of wind with wavelength ~ 1300 km at 500 hPa or above was turned on.

To evaluate the effectiveness of spectral nudging in improving the downscaled results, all extreme cases (~ 45 cases) in the GFDL-ESM2M historical and RCP 8.5 runs were downscaled in the outermost domain (d01) with and without spectral nudging. Then the room-mean-square error (RMSE) of hourly rain rate in WRF relative to GFDL-ESM2M data was calculated as:

$$\text{RMSE [mm]} = \sqrt{\sum_{i=1}^{n_j} \frac{\left(\text{Rain}_{\text{WRF}\,j_i}[mm] - \text{Rain}_{\text{ESM2M}\,j_i}[mm]\right)^2}{n_j}}$$

where j = 1 or 2 representing different climate scenarios, i is the extreme case number and n_j is the total number of extreme cases. The RMSE of in 50 historical climate extreme cases are 0.772 mm without nudging, and is reduced to 0.598 mm if nudging is used. For 57 cases in RCP 8.5, the RMSE decreased from 0.953 mm to 0.752 mm. Spectral nudging reduces the RMSE by ~ 20 % for both historical and RCP 8.5 runs.

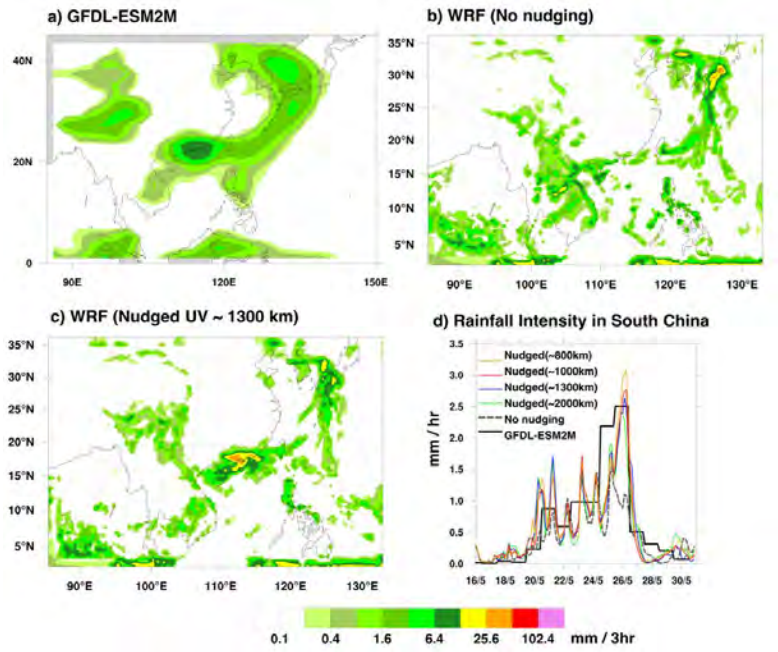

Figure 2.7 *(a-c) Snap shot of rainrate during one selected extreme case from (a) GFDL-ESM2M historical run, (b) WRF-downscaled result without nudging and (c) WRF-downscaled results with U- and V-wind spectrally nudged from GFDL-ESM2M of wavelength ~ 1300 km. (d) Area-averaged rainrate over south China simulated by GFDL-ESM2M (black solid), WRF result without nudging (grey dotted), WRF result with nudged U- and V- wind of wavelength ~ 2000 km (green solid), ~ 1300 km (blue), ~ 1000 km (red solid) and ~ 800 km (orange solid).*

3. Results

3.1. GFDL-ESM2M model evaluation

McSweeney et al. (2015) assessed 28 CMIP5 model simulations and concluded that GFDL-ESM2M performs well over south east Asia (see section 2.2). Over the region of 15 to 50 ºN, 90 to 140 ºW, the GFDL-model products including temperature (T_a), geopotential height (H), U-wind (U_a) and V-wind (V_a) were compared with ERA-Interim reanalysis data from the European Centre for Medium-Range Weather Forecasts (ECMWF) (Dee et al., 2011). Precipitation (Pr) rates are compared with the Tropical Rainfall Measuring Mission (TRMM) multi-satellite 3B42 product with 0.25º x 0.25º resolution provided by Tropical Rainfall Measurement Mission Project from Goddard Space Flight Center Distributed Active Archive Center (Huffman et. al, 2015). **Table 3.1** summarize the observational and model data used for model evaluation. The observation data were re-gridded into the same resolution as for the GFDL-ESM2M products before any calculations.

	GFDL-ESM2M Model		**Observation**	
	Historical	*RCP 8.5*	*TRMM-3B42*	*ERA-Interim*
Time period	60 yrs	95 yrs	1998 – 2013	1979 – 2014
Variables	T_a, H, U_a, V_a and Pr		Pr	T_a, H, U_a and V_a
Spatial resolution (lat × lon)	2.5º × 2.0º		0.25º × 0.25º	1.5º × 1.5º
			(Re-gridded into 2.5º × 2.0º)	

Table 3.1 *Summary table of model data and observational data used*

3.1.1. Systematic biases

Biases of model monthly mean products were computed on a grid-by-grid basis. **Figure 3.1** gives the monthly mean values of variables T_a, H, U_a, V_a and Pr from ESM2M versus those from observations. It can be seen that GFDL-ESM2M gives ~ 1 K (1.2 – 5 K) systematic underestimation of near-surface (mid-tropospheric) temperature. Such cold biases lead to an underestimation of geopotential height from 5 m to 130 m in the mid to upper troposphere (see **Figure 3.1 b** and **Figure 3.2 b**). On the other hand, u-wind and v-wind are simulated well by ESM2M throughout the whole troposphere. **Figure 3.2 c** shows that the 850 hPa wind in GFDL-ESM2M can capture the western Pacific subtropical high and the monsoon circulation from equator to the South China Sea. Lastly, **Figure 3.1 e** and **Figure 3.2 d** also show that the model rainfall distribution and intensity do not simulate well compare with observations, with an underestimation over southern China. Therefore, the extreme cases selected maybe less intense than the actual rainfall intensity in PRD. **Figure 3.2 d** shows that ESM2M can capture the large-scale rainfall systems well such as the Meiyu-Baiu rainband from central China to Japan. In general, GFDL-ESM2M still performs reasonably well in reproducing the summertime circulation in East Asia.

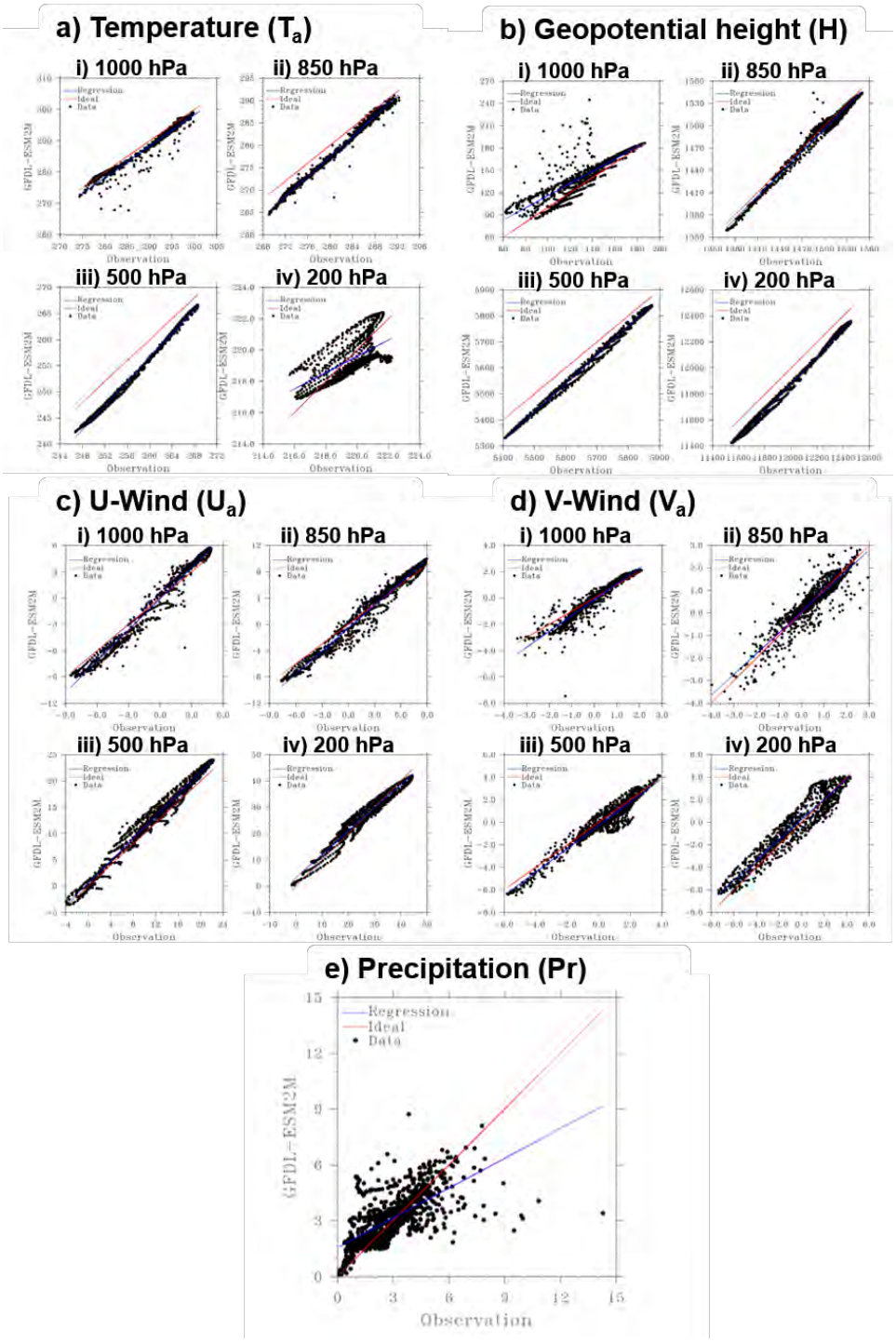

Figure 3.1 *Biases scatter plots for variables: (a) temperature (T_a), (b) geopotential height (H), (c) u-wind (U_a), (d) v-wind (V_a) and (e) precipitation (Pr) in MJJAS monthly climatology. For T_a, H, U_a and V_a, the plots are sub-plotted in (i) 1000 hPa, (ii) 850 hPa, (iii) 500 hPa and (iv) 200 hPa. Values computed in GFDL-ESM2M are plotted at y-coordinate and observations (ERA-Interim, TRMM-3B42) are plotted at x- coordinate. Blue lines are the regression lines for the scatter plots and red lines are the lines indicating ESM2M model result identical to observation. See text for details. Units of temperature: K, geopotential height: m, U- and V-wind: m s^{-1} and precipitation: mm day^{-1}.*

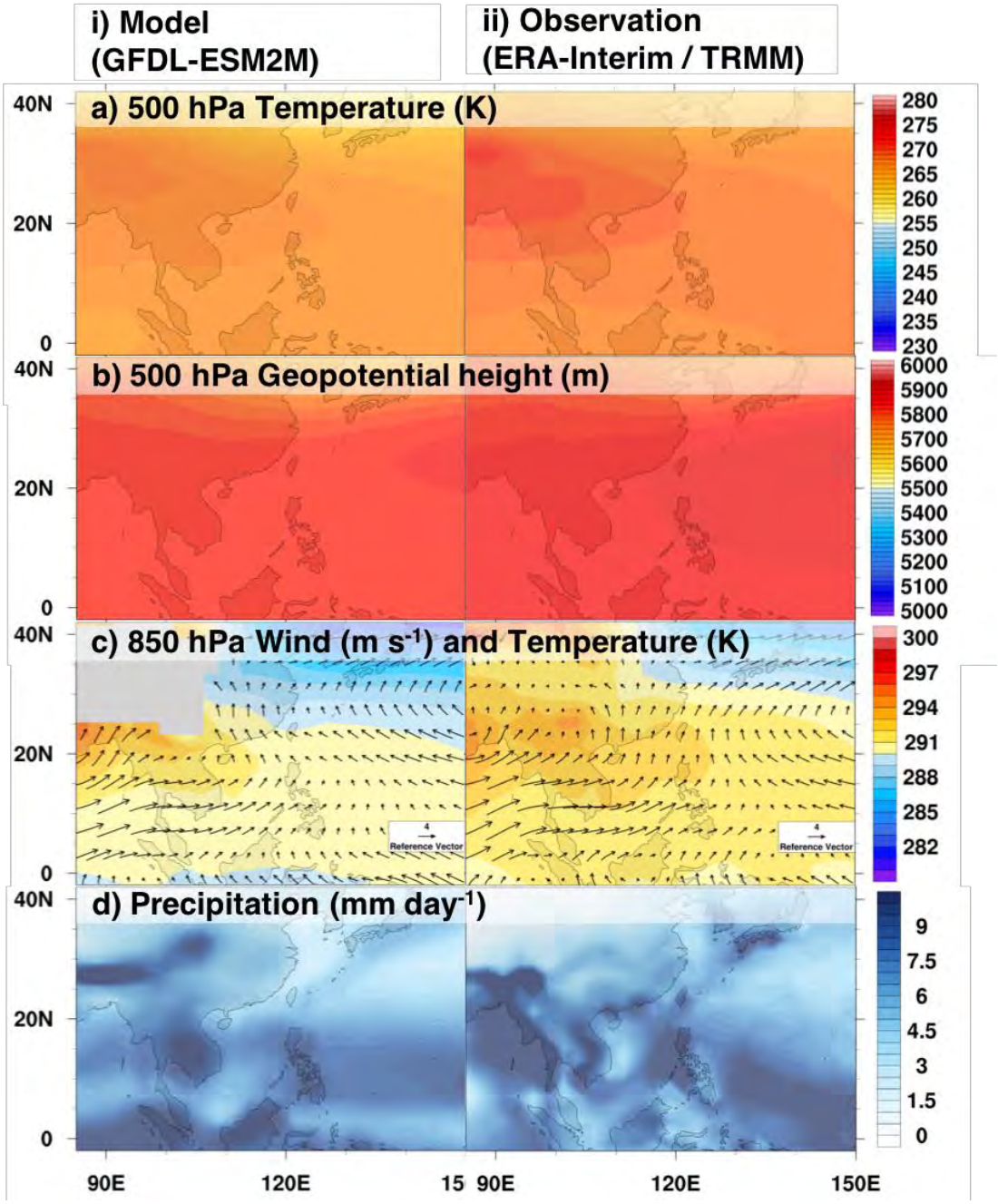

Figure 3.2 *Climatological seasonal mean (MJJAS) of (a) 500 hPa temperature, (b) 500 hPa geopotential height, (c) 850 hPa wind circulation overlaid on 850 hPa temperature and (d) daily precipitation amount at the (i) GFDL-ESM2M historical and (ii) observations (ERA-Interim for atmospheric variables or TRMM-3B42 for precipitation).*

3.1.2. Atmospheric variability

Besides evaluating the amplitudes of various meteorological variables, their patterns are also examined within the same region. Taylor diagrams are used to describe their pattern correction and RMSE (Taylor, 2005) compared with the observations. **Figure 3.3 a** to **d** show that temperature, geopotential height, u-wind are relatively well simulated, especially in the boreal summer period (with correlation coefficient ≥ 0.8 and standardized deviation of 0.6 – 1.4). Precipitation is not well reproduced, in comparison, with pattern correlation coefficient of 0.6 only.

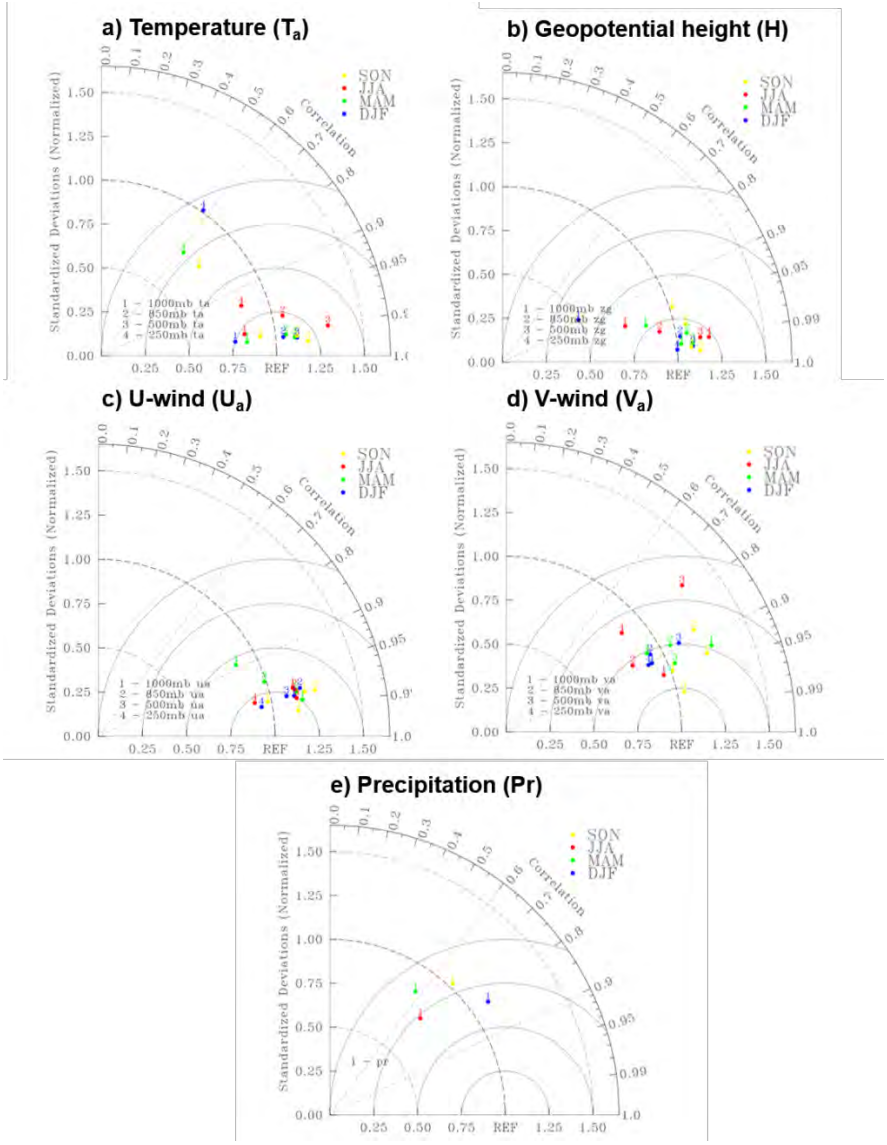

Figure 3.3 *Taylor diagrams for (a) temperature (T_a), (b) geopotential height (H), (c) u-wind (U_a), (d) v-wind (V_a) and (e) precipitation (Pr) from GFDL-ESM2M, averaged over different seasons. Values are compared between GFDL-ESM2M and observations (ERA-Interim for atmospheric variables and TRMM-3B42 for precipitation).*

3.2. GFDL-ESM2M climatology for historical and RCP 8.5 simulations

The GFDL-ESM2M projected changes of East Asia to western north Pacific summertime conditions from historical climate to RCP 8.5 are now examined. There are obvious differences in temperature, geopotential height, wind, precipitation etc. between RCP 8.5 and historical climate runs. **Figure 3.4** shows the precipitation, 850 hPa wind circulations and surface temperature in both climates runs. Anomalous warming of surface temperature by ~ 1.5 K is found over both ocean and land. From the circulation pattern, **Figure 3.4 a** and **c** show that southern China is under the influence of the subtropical high over the western north Pacific and monsoon circulation from the Indochina and Philippines. **Figure 3.4 e** shows the changes in RCP 8.5 run relative to historical run. North-easterly anomalies is found at southern China indicating a weakened subtropical high, hence creating an anomalous cyclonic flow from south-eastern China to Taiwan. The precipitation pattern shows an insignificant decrease in accumulated precipitation over the southern China in RCP 8.5 (see **Figure 3.4 f**).

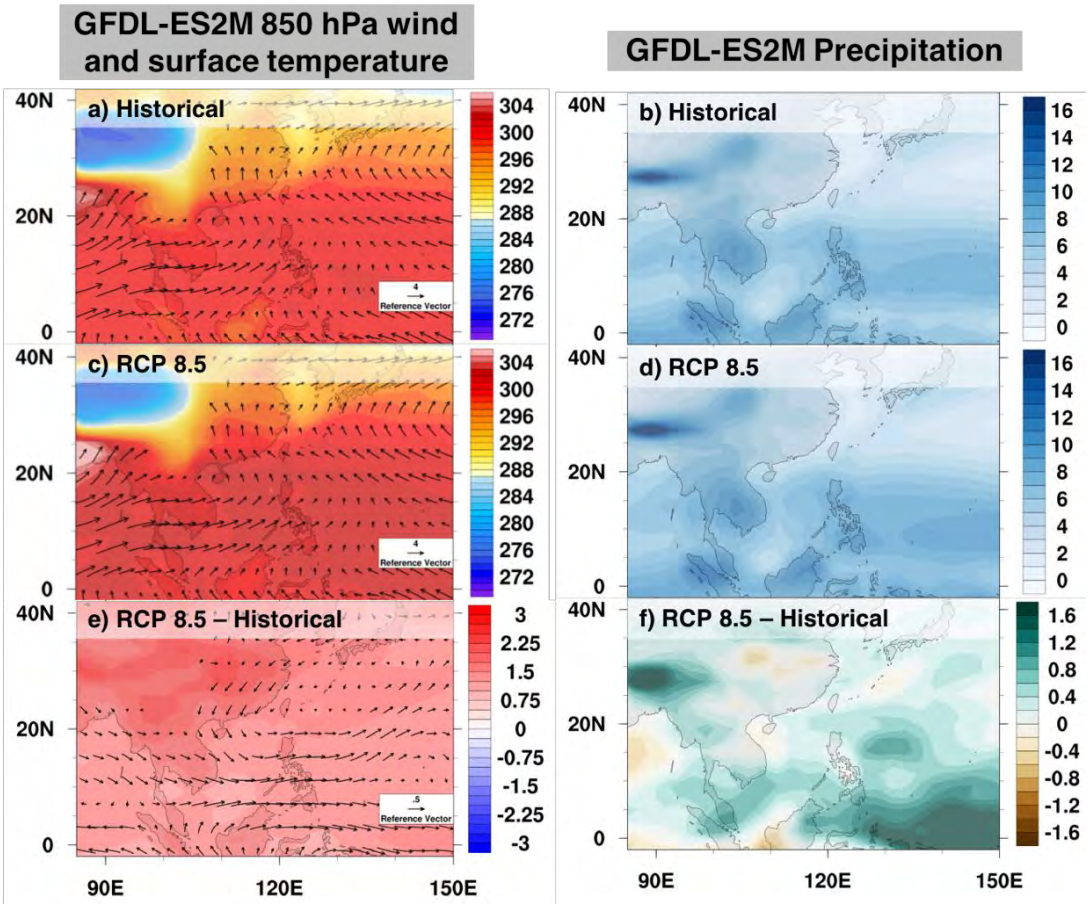

Figure 3.4 *The MJJAS meteorological conditions in GFDL-ESM2M (a, b) historical, (c, d) RCP 8.5 run and (e, f) the difference between historical and RCP 8.5. For subplots (a, c, e) shading is the surface temperature (units: K) and vectors are 850 hPa wind circulation (units of scale arrow: m* s^{-1}*) and subplots (b, d, f) is precipitation (units: mm* day^{-1}*) in the extended summer period (MJJAS).*

3.3. Rainfall characteristics in GFDL-ESM2M

3.3.1. Climatological rainfall statistics

After evaluating global warming's effect on the seasonal mean circulation, the GFDL-ESM2M daily rainfall characteristics in Southern China is further investigated. In the region over which extreme cases are identified (17 – 27 ^{o}N, 105 – 117 ^{o}E; see **Figure 2.1**), statistics of daily rainfall during all wet days ($\geq$ 0.1 mm day^{-1}) are computed (see **Figure 3.5**). Section 3.1.1 has already shown that GFDL-ESM2M has a dry bias over the southern China when compared with TRMM-3B42. **Figure 3.5** shows the GFDL-ESM2M daily rain rates that reach 30th percentile or above are less intense than the observation which leads to an underestimation in southern China. The R99p values for GFDL-ESM2M historical run, RCP 8.5 run and TRMM-3B42 are 16.7, 18.3 and 23.8 mm day^{-1}, respectively (dotted lines in **Figure 3.5**). Thus R99p is enhanced by 9.5 % in the RCP 8.5 scenario compared to the present climate. Other extreme indices also show increments in the RCP 8.5 scenario, such as the 95th percentile (R95p) and the simple daily intensity index (SDII) with magnitude of 5.8 % and 4.5 %, respectively. In GFDL-ESM2M, the near surface temperature in southern China is enhanced by ~ 1.5 K. The enhancement of R99p roughly follows the CC relationship (6.3 % K^{-1}), while R95p (5.8 % K^{-1}) and SDII (3 % K^{-1}) have a sub-CC relationship.

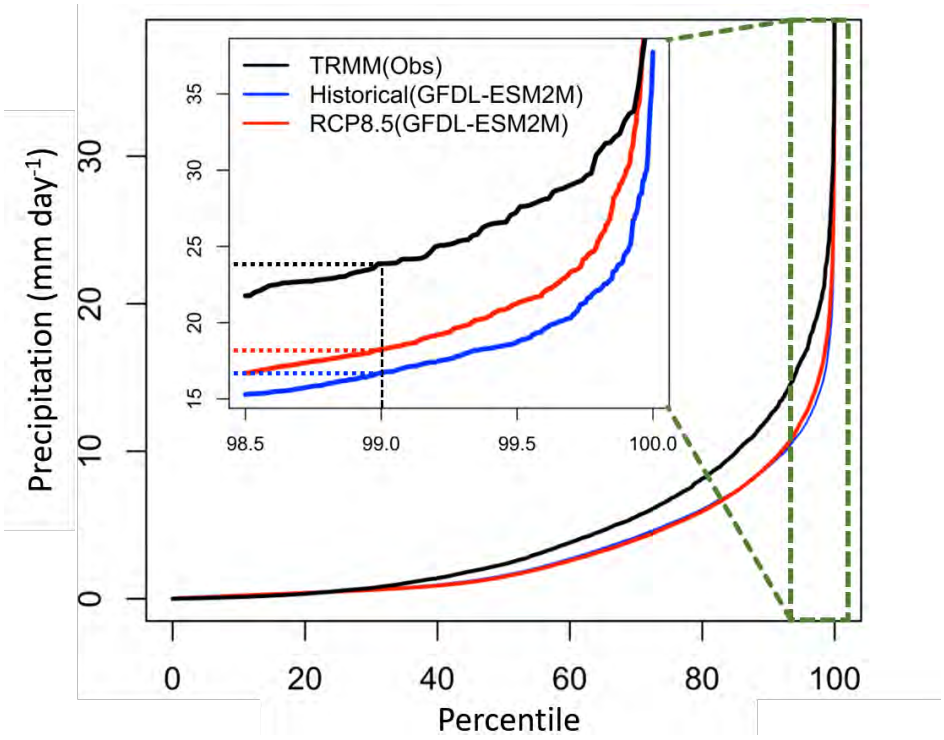

Figure 3.5 *Percentile plot of spatial averaged precipitation over 17º – 27 ºN, 105 – 117 ºE from GFDL-ESM2M historical run (blue), GFDL-ESM2M RCP 8.5 run (red) and TRMM-3B42 (black). Only statistics of wet day (daily rainfall > 0.1 mm day^{-1})*

SDII is more useful to for comparing the yearly rainfall conditions instead of identifying daily extreme cases. Instead, R95p, R99p and R99.9p are more relevant for identifying short-term extreme rainfall cases. **Figure 3.6** shows the monthly distribution of cases that exceed R95p, R99p and R99.9p thresholds. For those based on R95p and R99p, a peak of number of cases is found around June to July. There are 89 % (86 %) of cases happened in extended boreal summer when using R95p as cut-off value in the historical (RCP 8.5) run (similar results for R99p). However, the distributions of R99.9p are noisier (see **Figure 3.6 c**), and therefore R99.9p was not considered to be the threshold for extreme events identification. Instead, R99p is chosen as a threshold value to identify heavy rainfall cases in the GFDL-ESM2M simulations.

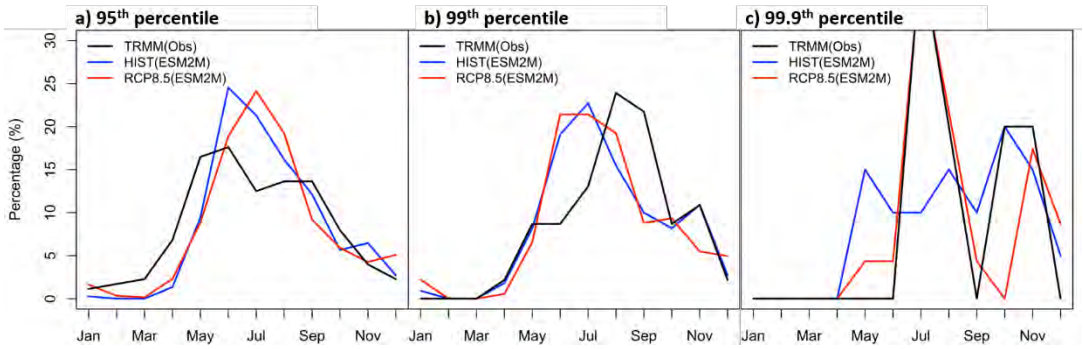

Figure 3.6 *Monthly distribution of extreme rainfall cases occurrence using (a) 95th percentile, (b) 99th percentile and (c) 99.9th percentile of daily rainfall as threshold for identification in GFDL-ESM2M's historical run (blue), RCP 8.5 run (red) and TRMM-3B42.*

Figure 3.5 has already shown that in the RCP 8.5 scenario extreme rainfall intensity over southern China will be stronger than that in the historical run. This result is further verified by comparing extreme events occurrence frequencies in the historical and RCP 8.5 simulations using historical run's R99p as threshold. In order to smooth out the inter-annual variability, the running 5-year sum of occurrences is given in **Figure 3.7**. On average, the historical climate gives 6.9 extreme rainfall cases with intensity > 16.7 mm day^{-1} every 5 years, while the RCP 8.5 scenario has 10.5 extreme cases, implying an increase of 52%.

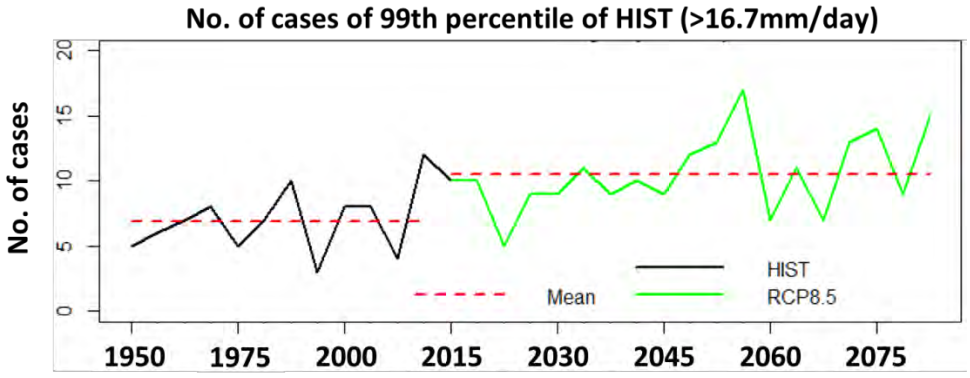

Figure 3.7 *Number of extreme rainfall cases per 5 years in GFDL-ESM2M historical climate (black) and RCP 8.5 scenario (green) identified using the historical R99p as a threshold.*

3.3.2. Composite correlation

After evaluating the general rainfall conditions in both climate scenarios, composites of the GCM circulation during extreme rainfall events are presented. **Figure 3.8** shows the GFDL-ESM2M 850 hPa wind circulation and precipitation composites for selected non-TC and TC cases from the historical and RCP 8.5 simulations. Comparing **Figure 3.8 c** and **f**, both non-TC cases and TC cases selected indicate enhancement of rainfall intensity over the southern inland China at 20°N and extending to the East China Sea, and also the suppression of rainfall at 30°N and the South China Sea due to global warming. The dry zone found over South China Sea in both non-TC and TC extreme rainfall cases is consistent with the change in climatological rainfall in **Figure 3.4 f**. This dry zone suggests that global warming effect on rainfall intensity will be milder than that expected based on the CC-relation. This explains why most extreme indices evaluated over southern China in section 3.3.1 are changing according to sub-CC relationship.

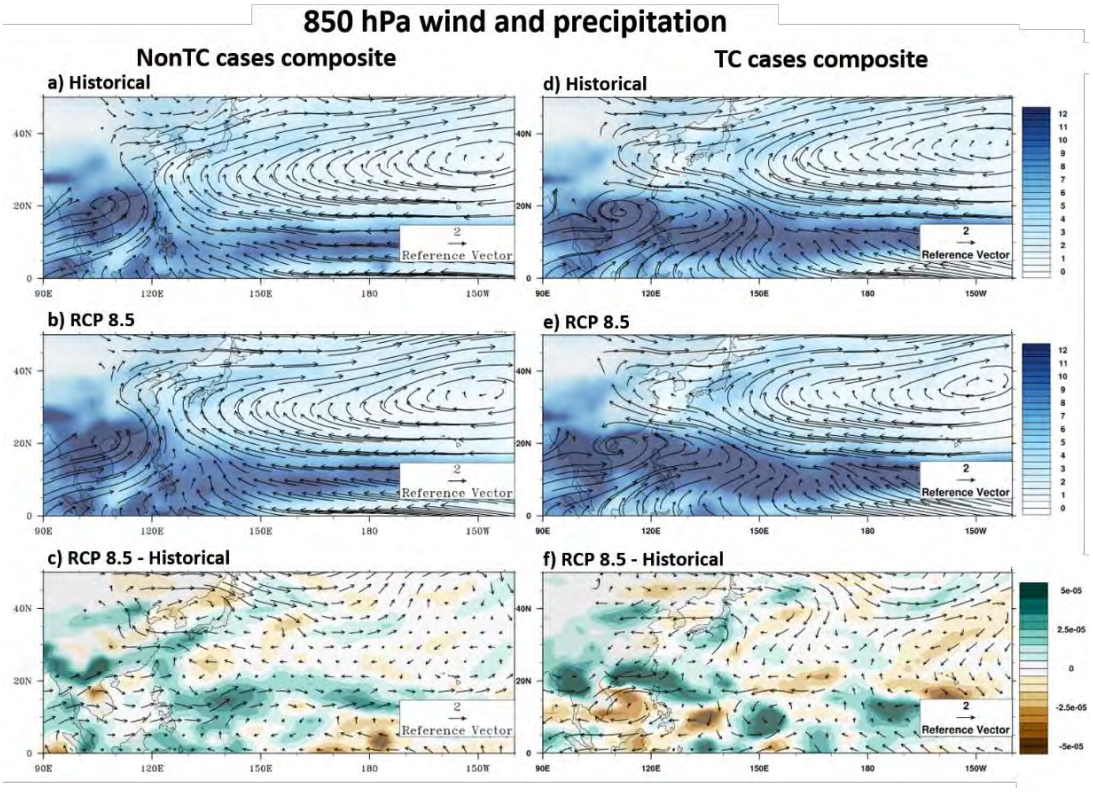

Figure 3.8 *Composite of GFDL-ESM2M 850 hPa wind circulation (arrows; units: m s^{-1}) and precipitation (shading; units: mm day^{-1}) for selected (a – c) non-TC and (d – f) TC extreme cases in (a, d) historical and (b, e) RCP 8.5 runs. (c, f) show the difference between RCP 8.5 and historical simulations. Vectors are the wind circulation with units: m s^{-1} and shading is the precipitation with units: mm day^{-1}.*

3.4. Results from dynamically downscaled non-TC cases

Dynamical downscaling of non-TC cases results are first considered. The results in this section are based on 26 downscaled non-TC extreme rainfall cases identified in historical runs and 27 cases for RCP 8.5 runs. For each of these identified cases, two downscaling experiments were carried out: one with AH = 0 W m^{-2} and the other with 300 W m^{-2} (see section 2.4.2.1). The urban heating effect is examined from the difference between HIST_AH300 and HIST_AH0, the heating effect for RCP 8.5 between RCP85_AH300 and RCP85_AH0 is also compared. The global warming effect can be inferred by comparing RCP85_AH0 and HIST_AH0, also by comparing between RCP85_AH300 and HIST_AH300 for urbanized conditions (see **Table 2.1** for experiments conducted).

3.4.1. Impacts on time-mean rainfall during extreme events

The mean rainfall changes are computed by time averaging downscaled results in d03 taken from the selected non-TC cases (see **Figure 3.13**). Averaging in time and over a substantial number of cases in each experiment can lead to more robust statistics due to better sampling. From **Figure 3.9 a** and **b**, the urban heating effect poses similar impacts on both historical and RCP 8.5 simulations, with enhancement of mean precipitation by ~ 0.7 mm hr^{-1} (~ 20 %) over the urban area. Over the whole d03 domain, the mean rainfall is enhanced by ~ 0.17 mm hr^{-1} (~ 6.7%). Mean rainfall enhancement is mainly found over the urban area.

From **Figure 3.9 c** and **d** the global warming effect changes the whole d03 mean rainfall ranging from -0.069 to 0.028 mm hr^{-1} (-1 to 3%). Notice that there is a dry anomaly along the coast of PRD; this is consistent with the GCM result in **Figure 3.8 c**, with dryer conditions over southern China in the RCP 8.5 scenario compared with the historical run. The results suggest that AH can enhance the mean rainfall, especially over the urban area, while global warming may or may not enhance the mean precipitation depending on the GCM outputs.

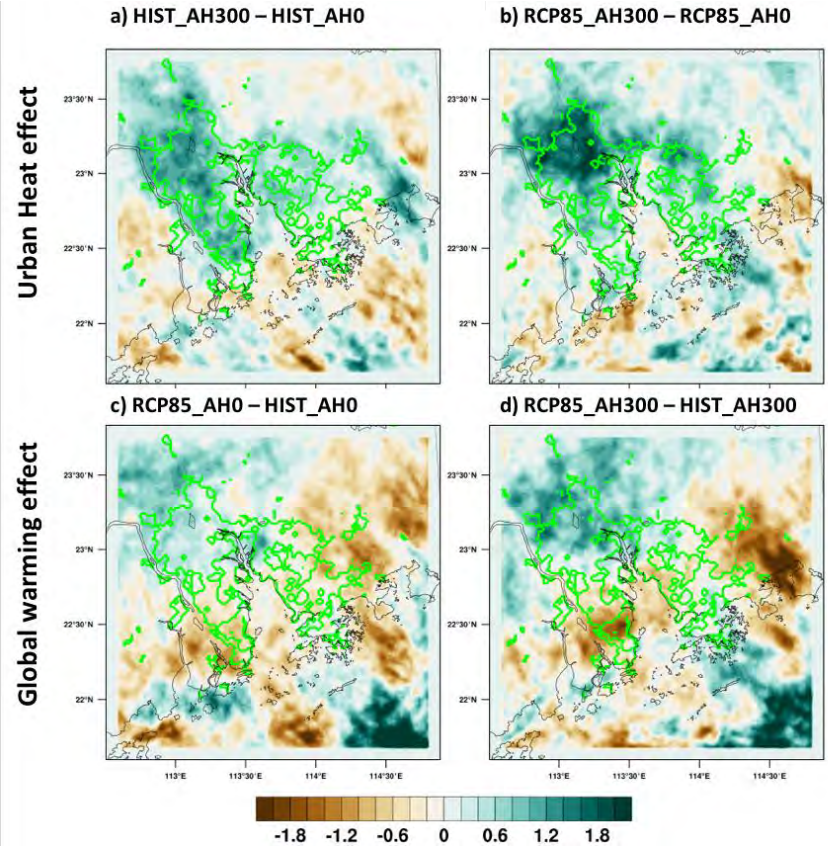

Figure 3.9 *The change of mean rainfall in d03 between (a) diurnal peak AH of 300 W m^{-2} and 0 W m^{-2} at GFDL-ESM2M historical run, (b) peak AH of 300 W m^{-2} and 0 W m^{-2} at GFDL-ESM2M RCP 8.5 run (c) GFDL-ESM2M RCP 8.5 and historical run downscaled by WRF with peak AH of 0 W m^{-2}, and (d) GFDL-ESM2M RCP 8.5 and historical run downscaled by WRF with peak AH of 300 W m^{-2}. All values are computed by time averaging downscaled results from d03, and by averaging over selected of non-TC heavy rainfall cases identified in the GFDL-ESM2M simulations. The green lines labelled the boundaries of urban area in d03. Units: mm hr^{-1}. See text for details.*

3.4.2. Rainfall characteristics

Hourly rainfall rates from the downscaling experiments is further examined based on the downscaled non-TC results. Hourly precipitation intensity in every grid box over both urban and non-urban locations in d03 from all non-TC extreme cases were used to compute rainfall PDFs with 10 mm hr^{-1} as the bin width (see **Figure 3.10**). **Figure 3.10 a** shows that the urban heating effect can lead to a decrease in the probability of light rain (< 10 mm hr^{-1}), but an increase in the probability of heavy rain (> 10 mm hr^{-1}) for the same climate scenario. Such shifting of rainfall PDFs mainly occurs in the urban grid boxes (see **Figure 3.10 b** and **c**). The global warming impacts on rainfall PDFs over both urban and non-urban area are not obvious in

Figure 3.10. For ease of comparison, the effect of AH is shown by computing the ratio of rain rates' probabilities in historical climate (HIST_AH300 to HIST_AH0) in **Figure 3.11 a** and RCP 8.5 scenario (RCP85_AH300 to RCP85_AH0) in **Figure 3.11 b**. Likewise, the global warming impact is also calculated as the ratio of rainfall probabilities for zero AH scenario (RCP85_AH0 to HIST_AH0) in **Figure 3.11 c** and AH = 300 W m^{-2} cases (RCP85_AH300 to HIST_AH0) in **Figure 3.11 d**.

It can be seen that as AH increases from zero to 300 W m^{-2}, probability of heavy rain ($\geq$ 10 mm hr^{-1}) is enhanced by ~ 25 % at 10 – 20 mm hr^{-1} to ~ 170 % at 80 – 90 mm hr^{-1} for both climate runs. On the other hand, probability of light rain (< 10 mm hr^{-1}) over urban area is reduced. Furthermore, the proportion of enhancement increases as the intensity of rain rate increases. Overall, the rainfall PDFs are shifted to the extreme side under the AH effect in both climate scenarios. Note that such results only apply over the urban grids. For the non-urban area, there is no significant change ($\pm$ 15 %) of the rainfall probability. Within d03, 72 % of the area is non-urban, therefore the rainfall PDFs for whole domain are dominated by the statistics over non-urban locations. Downscaled events are also evaluated individually. More than 90 % of cases demonstrated a shift in urban rainfall PDF, with higher probability of heavy rain rates due to the urban heat effect, which further confirmed the robustness of the AH effect on extreme rainfall.

The global warming effect for zero and non-zero AH are plotted in **Figure 3.11 c** and **d,** respectively. Global warming causes a wide region (i.e. over both urban and non-urban locations) with enhanced probability in heavy rain rate (> 20 mm hr^{-1}); however, the increase in urban area is greater. In particular, global warming increases the probability of heavy rain rates ($\geq$ 20 mm hr^{-1}) by ~ 10 % (for 20 – 30 mm hr^{-1}) to ~ 120 % (for 70 – 80 mm hr^{-1}) and reduces that for light rain (< 20 mm hr^{-1}) over the urban area. For non-urban locations, enhancement of probability of heavy rain rate ranging from ~ 5 % (for 20 – 30 mm hr^{-1}) to ~ 60 % (for 100 – 110 mm hr^{-1}), and the probability of light rain (< 20 mm hr^{-1}) is also reduced. From **Figure 3.9**, the mean rainfall already shows a dry zone over PRD especially in non-urban area; this probbaly lead to relatively less enhancement in the rainfall PDF.

KS tests can be carried out to determine if the two sets of distributions are distinct from each other. Here KS tests were used to see if the change of rainfall PDFs is significant. Every single grid points over d03, KS tests were applied to hourly rain rate PDFs. **Figure 3.12** shows locations (dotted) where the PDFs show

difference significant at the 90 % confidence level. The KS tests confirmed that AH effects mainly alter the rainfall PDF in the urban area (see **Figure 3.12 a** and **b**), while global warming result in rainfall PDF changes that are more wide spread and covers more than 50 % of the area in d03 regions (see **Figure 3.12 c** and **d**).

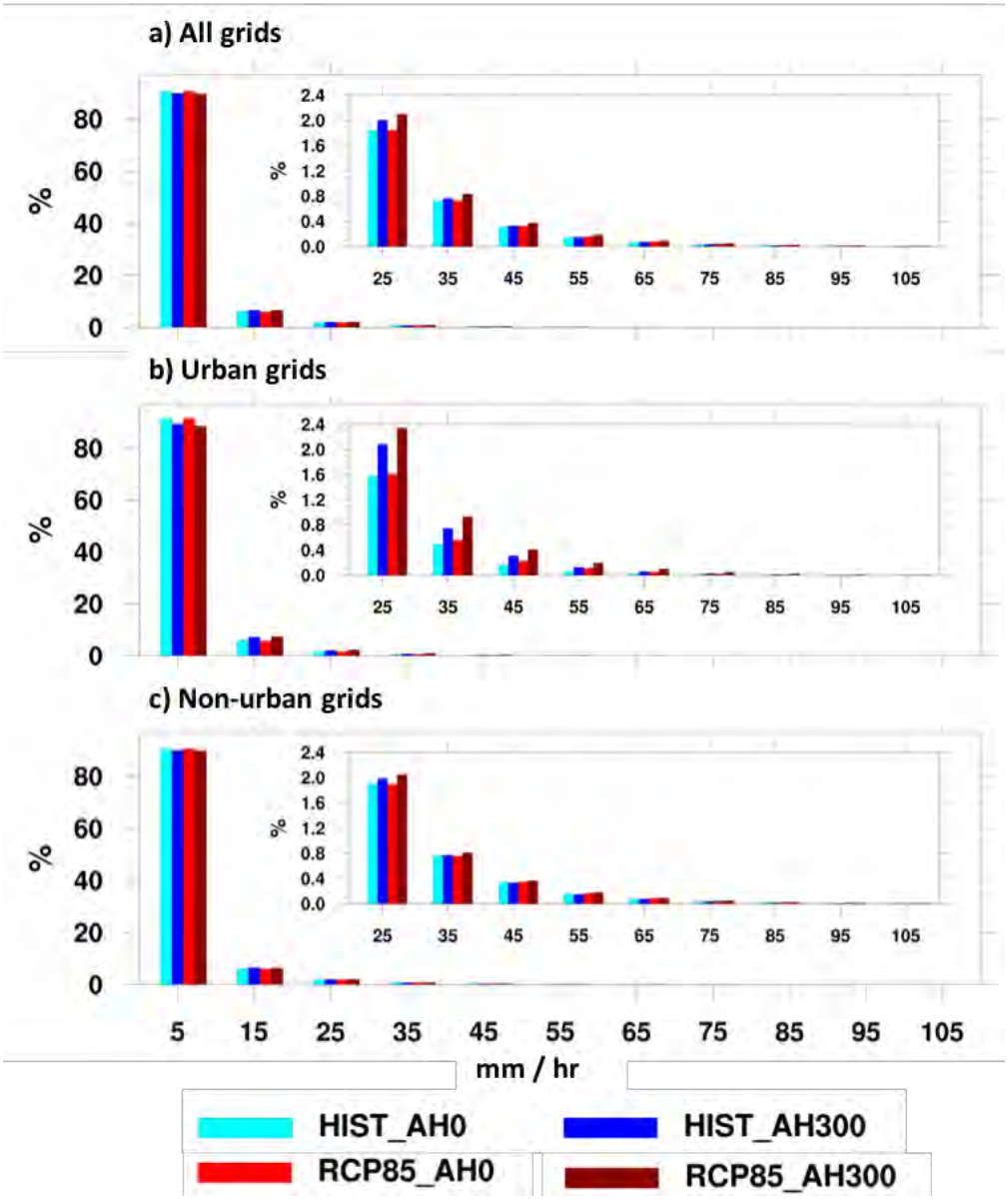

Figure 3.10 *PDFs of hourly rain rates in the ranges of 0-10, 20-30, 30-40, 40-50, 50-60, 60-70, 70-80, 80-90, 90-100 and 100-110 mm hr^{-1} in d03, computed based on outputs over (a) all grids, (b) urban grids and (c) non-urban grids by downscaling non-TC heavy rainfall cases from the GFDL-ESM2M historical run with zero AH (cyan), historical run with peak diurnal AH = 300 W m^{-2} (blue) RCP 8.5 zero AH (red) and RCP 8.5 simulations with peak diurnal AH = 300 W m^{-2} (dark red).*

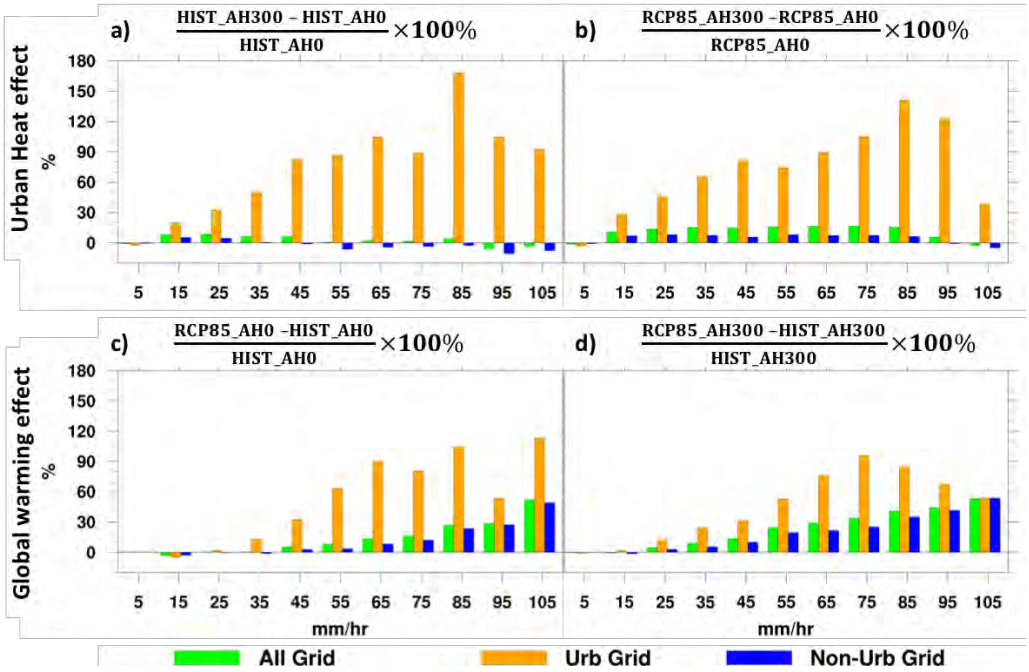

Figure 3.11 *Fractional change of hourly rain rate probability due to AH effect over urban (orange) and non-urban grids (green) in d03. (d) Same as (c) except for gauging global warming effect. See text for details.*

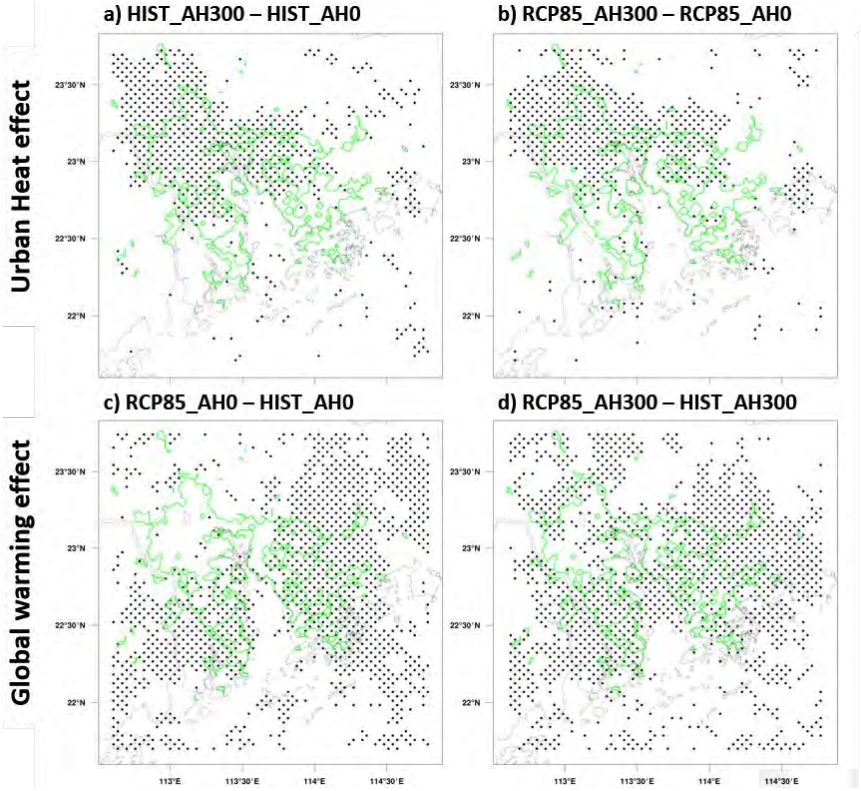

Figure 3.12 *KS test between (a) HIST_AH300 and HIST_AH0, (b) RCP_AH300 and RCP85_AH0, (c) RCP85_AH0 and HIST_AH0 and (d) RCP85_AH300 and HIST_AH300. The dotted regions indicated that p-value < 0.1.*

3.4.3. Impacts on time-mean temperature

3.4.3.1. 2m-temperature

AH in the urban area is expected to impact on near-surface temperature within the city. The mean 2m-temperatures are also computed using the same method as the time-mean rainfall in section 3.4.1 (see **Figure 3.13**). It is found that urban heat effect on 2m-temperature in historical (**Figure 3.13 a**) and RCP 8.5 runs (**Figure 3.13 b**) have similar patterns and intensities. With the presence of AH, the daily averaged urban 2m-temperature can reach up to 301 K and 303 K in historical and RCP 8.5 scenario, respectively. Note that the temperature enhancement is localized in the urban area (with magnitude of ~ 1.8 K); enhancement of ~ 0.15 K is found at the non-urban area in both climate scenarios. The enhancement of urban 2-m temperature was due to the AH released in SLUCM over the urban grids. The sharp boundary of 2m-temperature difference between urban and sub-urban area illustrates the heat is not advected or diffused into non-urban locations, hence there ia a temperature difference of ~ 3.4 K between urban and the non-urban area.

Global warming effect on 2m-temperture shows similar warming patterns and intensities for both zero AH (**Figure 3.13 c**) and 300 W m^{-2} peak AH runs (**Figure 3.13 d**). Warming is seen in wider region over which 2m-emperature is enhanced evenly over land by ~ 2.3 K, in both urbanization experiments. There is a slightly differential heating between the ocean and the land. Ocean is only heated up by ~ 2.1 K in both experiments.

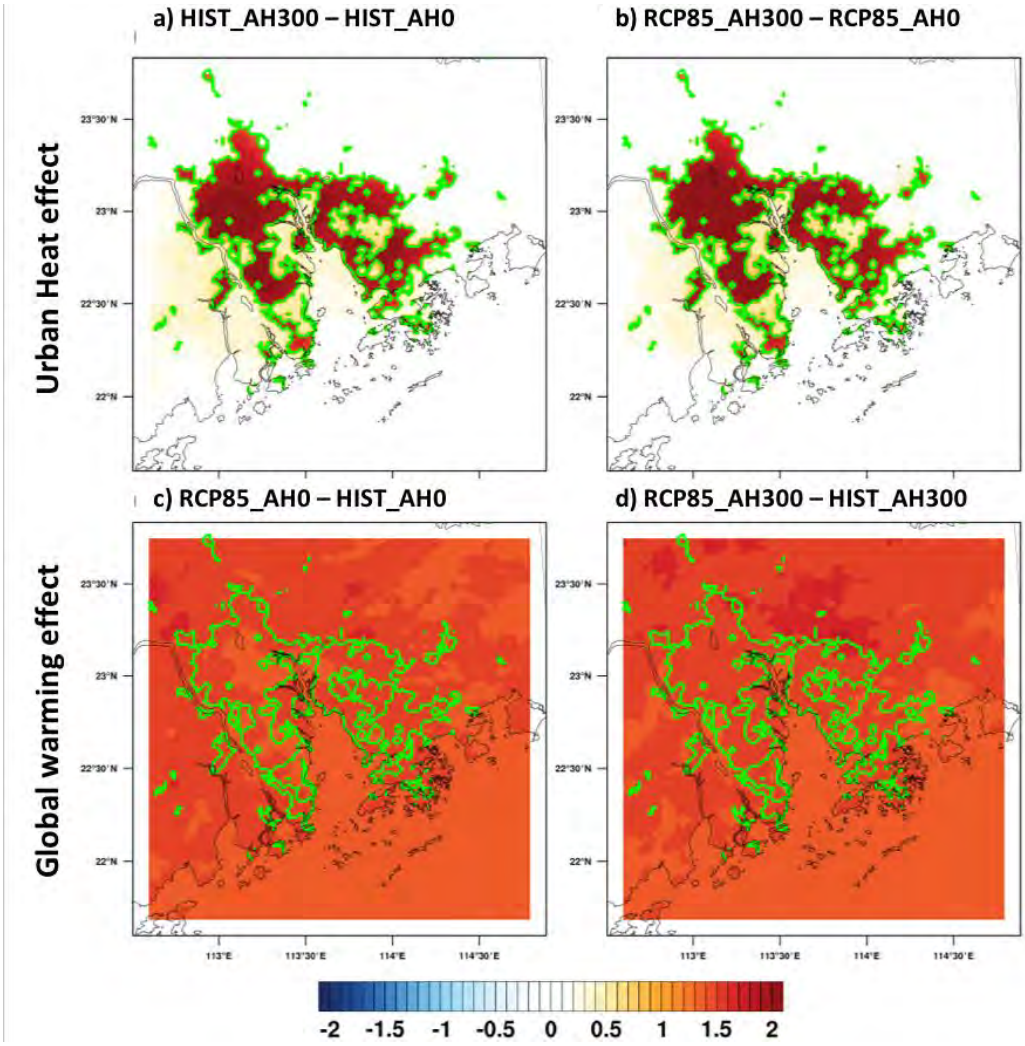

Figure 3.13 *Same as* ***Figure 3.9*** *plotting with the 2m-temperature changes in (a – b) AH and (c – d) global warming effect. Units: K.*

3.4.3.2. Vertical temperature profile

The vertical temperature profiles for different downscaling experiments over urban grids and non-urban grids are plotted in **Figure 3.14**. The vertical profiles show that AH enhances surface temperature at urban grids by ~ 1.8 K, which can be seen by comparing between (1) HIST_AH300 (blue) and HIST_AH0 (cyan) and (2) RCP85_AH300 (orange) and RCP85_AH0 (red). However, note that the AH impact can only warm up the atmosphere up to around 1.5 km vertically. On the other hand, under global warming, a raise in temperature is seen to extend to much higher levels in the troposphere.

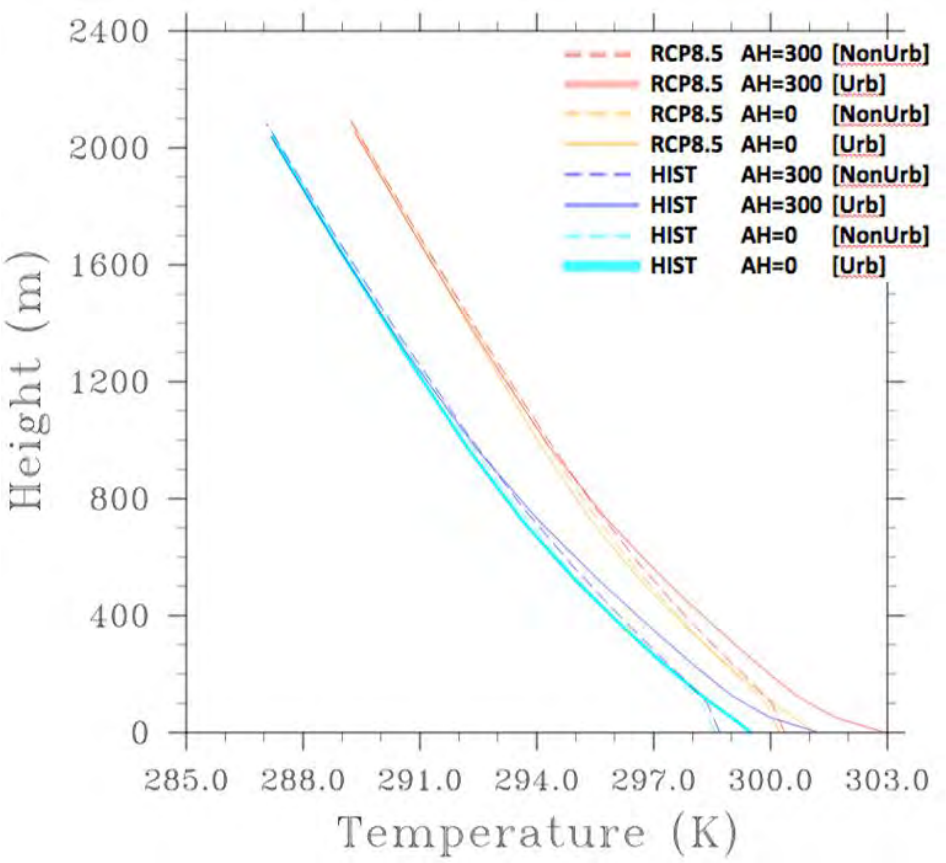

Figure 3.14 *The vertical temperature profile in the downscaled non-TC heavy rainfall cases from the GFDL-ESM2M historical run with zero AH (cyan), historical run with peak diurnal AH = 300 W m^{-2} (blue) RCP 8.5 zero AH (orange) and RCP 8.5 simulations with peak diurnal AH = 300 W m^{-2} (dark red). at non-urban area (dotted lines) and urban area (solid lines). All values are computed by time, spatial and cases averaging downscaled results from d03.*

3.4.4. Impacts on convective available potential energy and convective inhibition

Convective available potential energy (CAPE) is the amount of energy available for air parcel to carryout convection, while convective inhibition (CIN) is the amount of energy needed to lift an air parcel upward to the level of free convection (LFC). CAPE and CIN describe the energy available for convection and the barrier which needs to be overcome for convection to occur, and they are useful for indicating convective instability. CAPE values are calculated with averaging in time for non-TC cases and plotted in **Figure 3.15**. **Figure 3.15 a** shows that CAPE for urban is less than that in non-urban areas. This is likely due to the physical properties of different land surface; where natural vegetation is replaced by impervious urban surface, which reduces evapotranspiration. Hence, the value of CAPE also decreases (Yan et al., 2016). **Figure 3.15 b** shows that CAPE for urban area has similar magnitude as non-urban area when AH increases in urban locations. The effect of AH and global warming are also compared in **Figure 3.16**. It is seen that AH can enhance the surface temperature, leading to higher CAPE for convection in the urban area with an increment of 13.6 % (14.3 %) in historical (RCP 8.5) climate. **Figure 3.8** shows non-TC cases chosen in RCP 8.5 have anomalous easterly wind over PRD which illustrate the presence of stronger advection. CAPE in non-urban locations also slightly increase by 6.1 % in RCP 8.5, which is 4.2 % larger than that in the historical climate.

The effect of global warming can be evaluated in **Figure 3.16 c** and **d**. Over the whole d03 domain CAPE increases by ~ 20 %, meaning that its impact is comparable with the AH effect. Global warming warms up both land and ocean; the enhanced evapotranspiration thus also raises the value of CAPE (see **Figure 3.15**). Kunz et al. (2009) showed that CAPE for thunderstorm since 1974 to 2004 has an increasing trend which is consistent with the simulated results here. Furthermore, the moisture enhancement over ocean is more than land; therefore, increase in CAPE is more prominent over ocean (see **Figure 3.16 c** and **d**).

CIN values for different experiments are also plotted in **Figure 3.17**. CIN is reduced over urban area due to the difference of land use. Urban area has higher surface roughness, creating more turbulence which can dynamically destabilize the lower atmosphere; hence CIN is decreased. The effect of AH and global warming can be evaluated in **Figure 3.18**. AH significantly reduces CIN over urban locations by 24 % (14 %) and increases CIN in the sub-urban area by 9 % (20 %) in historical (RCP 8.5) scenario. The decrement of CIN over urban area is due to AH is smaller in RCP 8.5, while the increment over sub-urban area is more in RCP 8.5 climate. On the other hand, global warming's effect on CIN over the whole d03 domain is not robust. For zero AH runs, CIN is slightly reduced by 5 %, but in AH = 300 W m^{-2} runs, CIN is slightly enhanced by 2 %.

Overall, these results about CAPE and CIN suggest that AH can provide more heat and destabilize the lower atmosphere over the urban area. This explain why adding AH can result in higher probability of heavy rainfall in urban area only. Although CAPE increases slightly more due to non-zero AH in the historical climate, the induced CIN decrement is less. Therefore, the changes of rainfall PDFs in both climate scenarios are similar to each other. On the other hand, changes in CAPE and CIN due to global warming cover the whole model domain. Therefore, shifts of rain rates probability are found in both non-urban and urban locations.

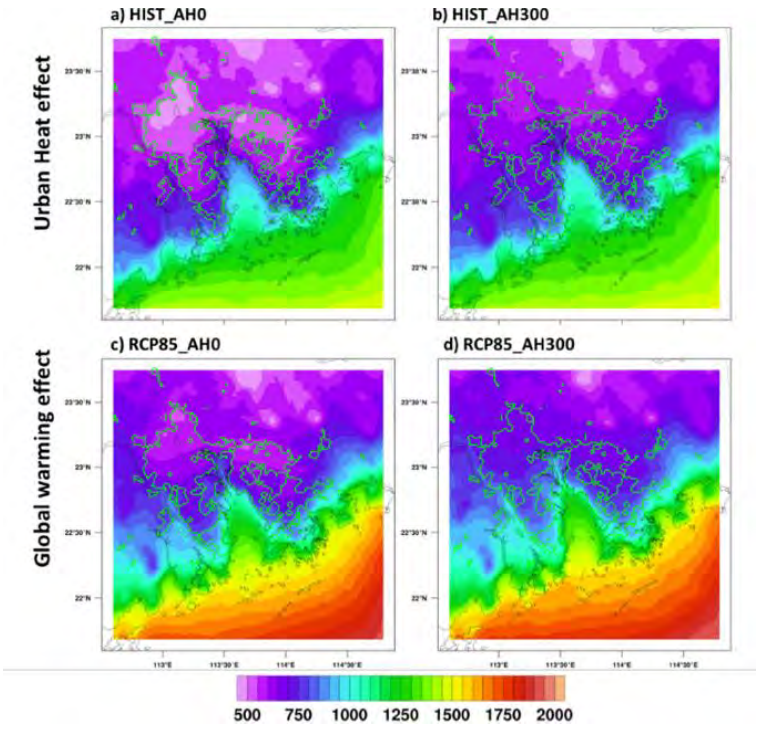

Figure 3.15 *CAPE in experiments (a) HIST_AH0, (b) HIST_AH300 (c) RCP85_AH0 and (d) RCP85_AH300. All values are computed by time averaging downscaled results from d03, and by averaging over selected non-TC heavy rainfall cases. Units: J kg^{-1}. The boundaries of urban area in d03 is marked by contours.*

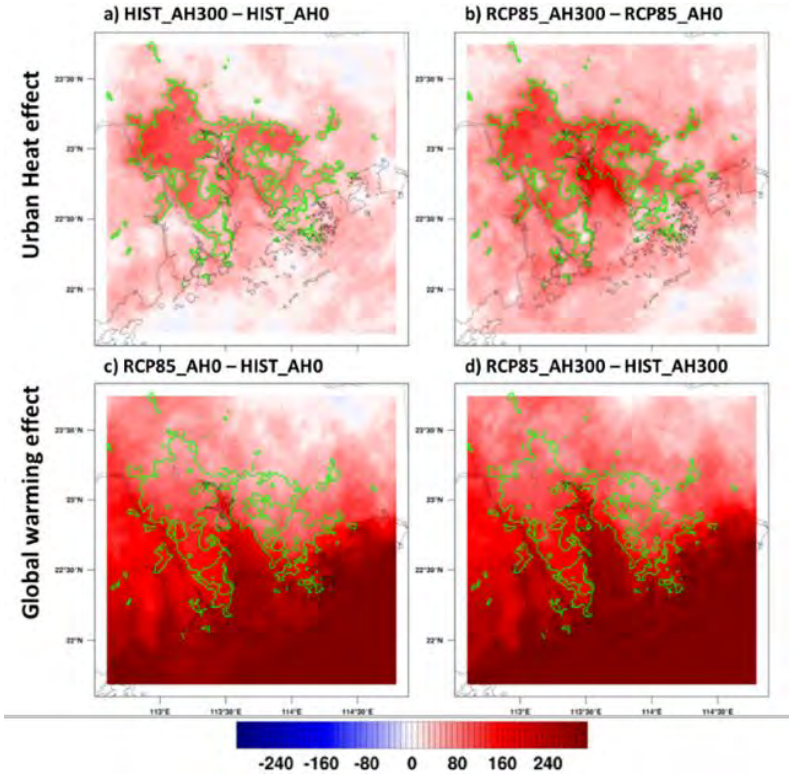

Figure 3.16 *Same as* ***Figure 3.9*** *plotting with the CAPE changes in (a – b) AH and (c – d) global warming effect. Units: J kg^{-1}.*

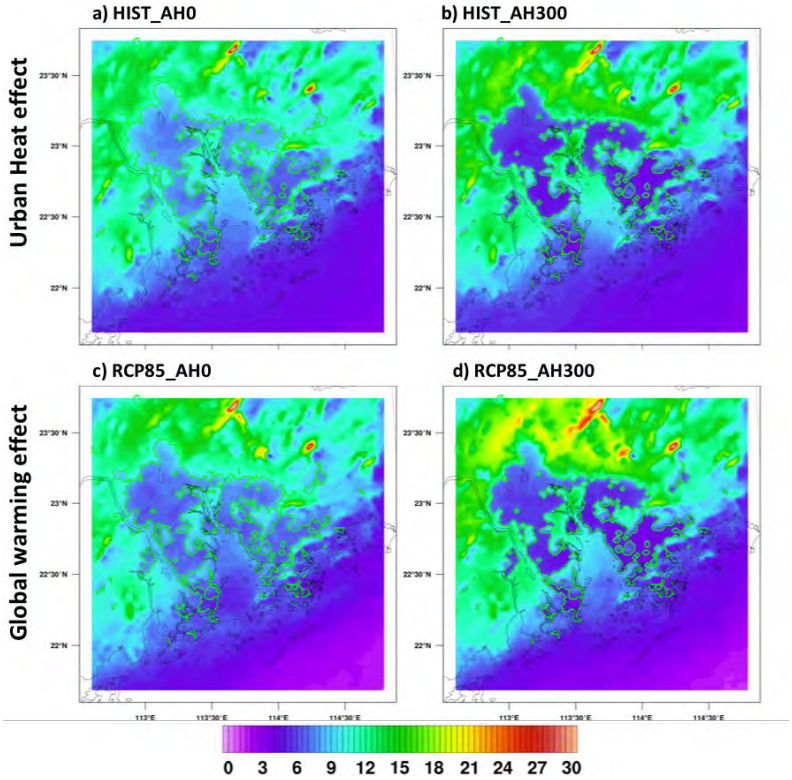

Figure 3.17 *Same as* ***Figure 3.15*** *plotting with the CIN. Units: J kg^{-1}.*

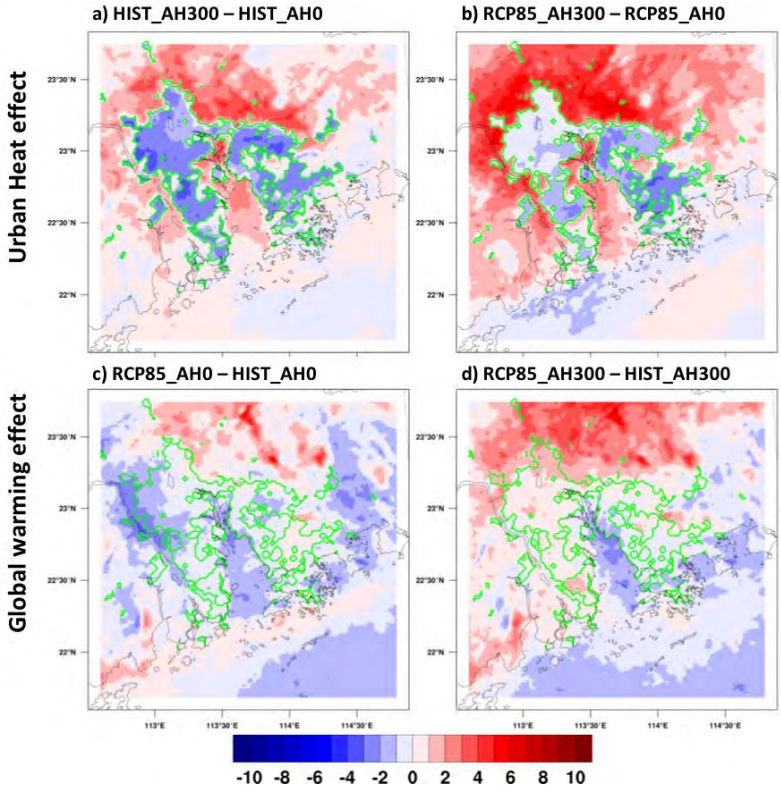

Figure 3.18 *Same as* ***Figure 3.9*** *plotting with the CIN changes in (a – b) AH and (c – d) global warming effect. Units: J kg^{-1}.*

3.4.5. Impact of AH on circulation above urban area

To further investigate the AH effect on the meso-scale circulation during non-TC extreme rainfall cases, vertical cross sections of the overturning circulation are plotted in **Figure 3.19**. Each non-TC extreme cases were simulated for zero AH and non-zero AH, and all experiments were averaged in time to construct composites of temperature, vertical wind speed and wind circulation. The difference between non-zero and zero AH experiments were analyzed in four directions: N to S, SW to NE, W to E and NW to SE centred at urban core.

The cross-sectional plots along these directions and experiments also show a warming zone just above the cities reaching ~ 1 km high. This UHI effect due to the presence of AH is consistent with **Figure 3.14**, i.e. the vertical temperature profile. Furthermore, for both climate scenarios there is enhanced vertical motion above the urban area. Anomalous vertical motion can be explained by the raised surface temperature, higher CAPE and also smaller CIN values in urban locations; hence, there is stronger convection and vertical motion. This consistent with the fact that enhancement in heavy rainfall probability and mean rainfall due to AH is mainly found in urban locations.

From the vectors in **Figure 3.19** the anomalous vertical motion over the city forms an overturning circulation with subsidence over the sub-urban locations. Such subsidence is consistent with enhanced CIN over the sub-urban (see **Figure 3.18 a** and **b**). Note that the AH impacts on the local circulation in historical and RCP 8.5 are not identical to each other, especially in the W to E direction. An anomalous downward motion is found to be closer to the city in RCP 8.5 climate. This may be due to the anomalous easterly wind over PRD region in RCP 8.5 compare with historical climate (see **Figure 3.8**). The stronger ventilation condition may weaken the local circulation induced by AH which causes suppressed mean rainfall on the eastern coast of PRD (see **Figure 3.9 b**). However, the wind speed difference is quite small, hence the difference between historical and RCP 8.5 climate may not be significant.

Overall, the presence of AH can destabilize the troposphere and induce stronger vertical upward motion above the city, creating more intense rainfall over the urban location.

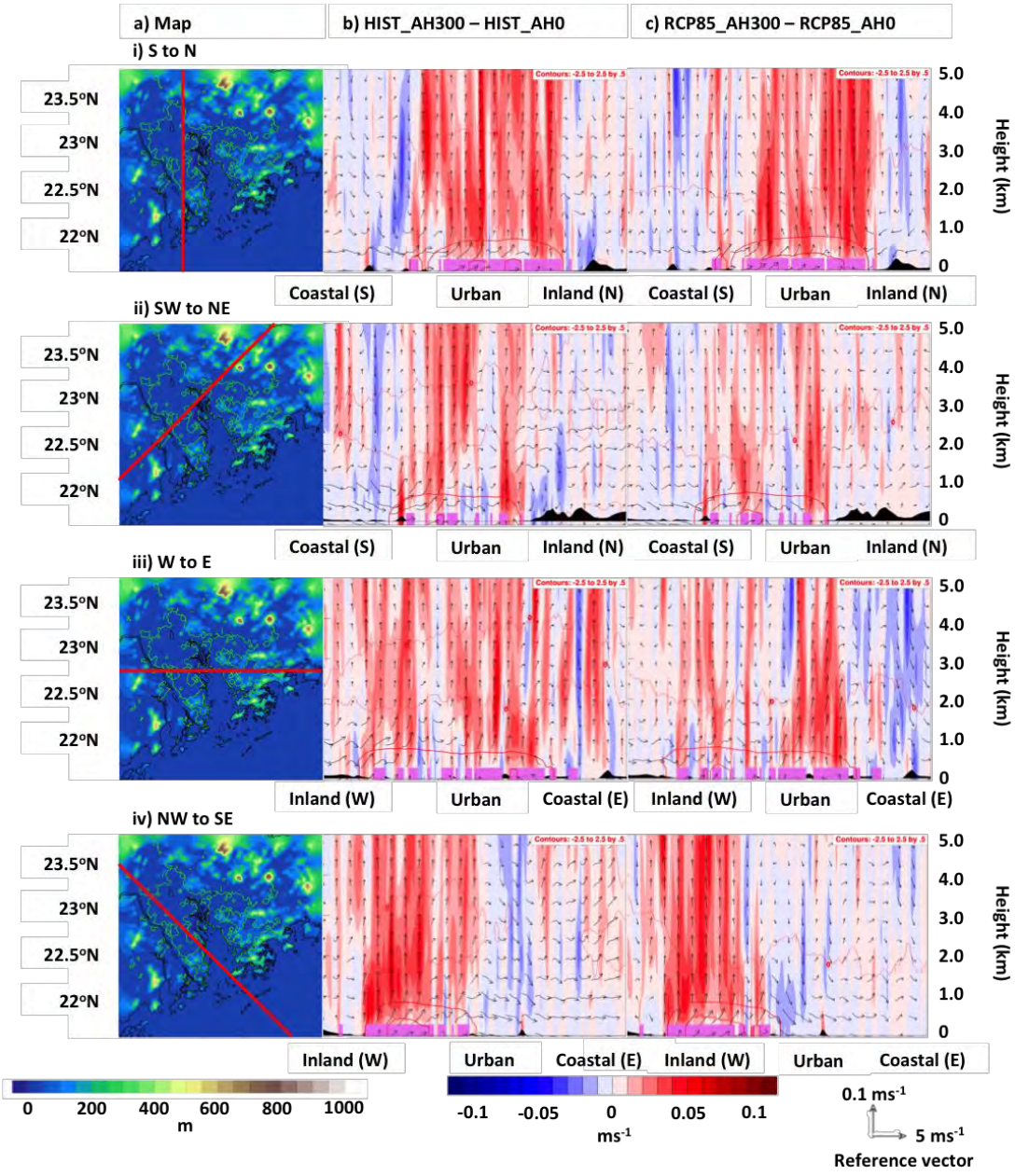

Figure 3.19 *Vertical cross section plot of wind circulation (vectors) and vertical wind speed (shaded) anomaly of downscaled non-TC extreme cases with prevailing wind direction in (i) N – S, (ii) NE – SW, (iii) E – W and (iv) SE – NW. (a) labelled the cross section line, (b) is the anomaly plot of AH effect at GFDL-ESM2M historical run (HIST_300 – HIST_0) and (c) is the anomaly plot of AH effect at GFDL-ESM2M RCP 8.5 run (RCP85_300 – RCP85_0).*

3.5. Results from TC cases

3.5.1. Impacts on time-averaged 2m-temperature

This section considers AH and global warming's impacts on TC-related heavy rainfall cases in PRD region. In terms of 2m-temperature, AH's effect for both historical and RCP 8.5 simulations have similar patterns and intensities (see **Figure 3.20 a** and **b**). With the presence of AH, the daily averaged urban 2m-temperature is enhanced locally in urban area by ~ 1.6 K. The differential heating in urban and non-urban area creates a difference of ~ 3 K temperature. This result is similar to that for the non-TC cases (see **Figure 3.13 a** and **b**). Global warming's effect on 2m-temperture is also similar to that for non-TC cases, with an increment of ~ 1.5 K in both urban and non-urban areas (see **Figure 3.20 c** and **d** and **Figure 3.13 c** and **d**).

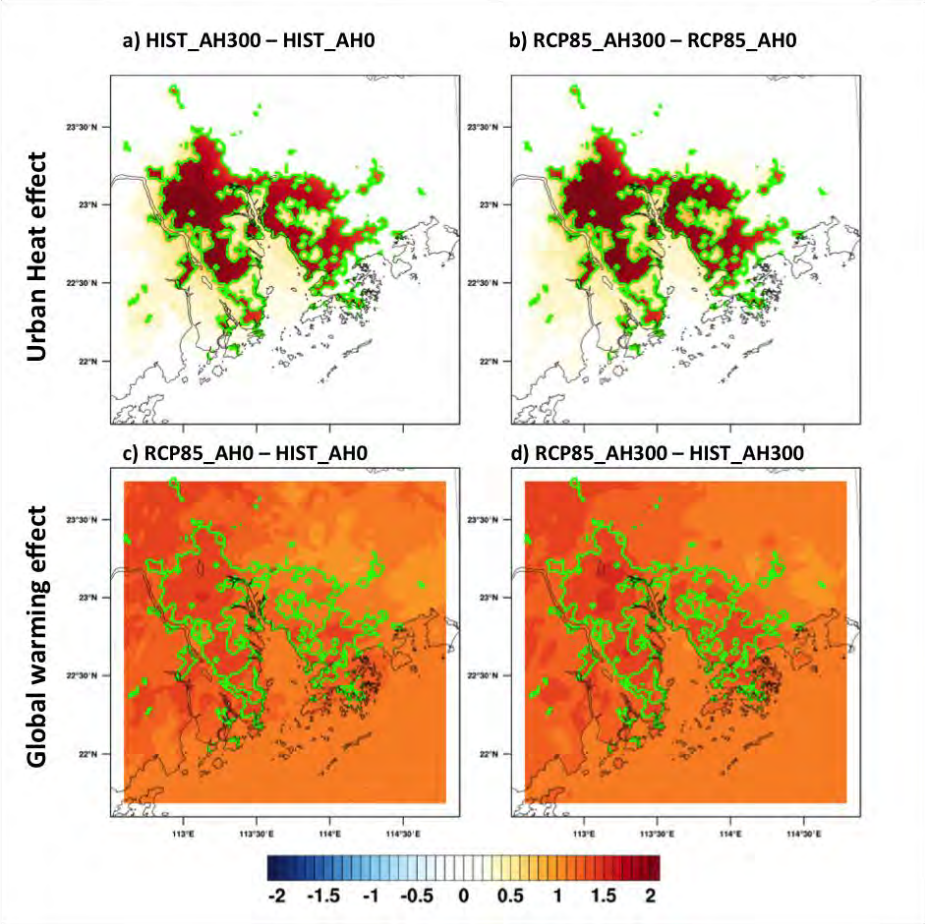

Figure 3.20 *2m-temperature of downscaled TC cases composite. (a) HIST_AH300 – AH0*

3.5.2. Impacts on time-averaged rainfall

Figure 3.21 displays the mean rainfall difference averaged over downscaled TC extreme rainfall cases in d03. **Figure 3.21 a** and **b** show that AH gives similar impacts in historical and RCP 8.5 runs. In the historical climate, mean rainfall in urban area is increased by 0.45 mm hr^{-1} (10.3 %) and over the whole domain also increased by 0.16 mm hr^{-1} (5.26 %). The RCP 8.5 scenario show similar magnitude of increment over the whole d03 domain by 0.11 mm hr^{-1} (4.49 %) and an increment of 0.16 mm hr^{-1} (3.68%) over the urban area. AH effect still enhances the TC mean rainfall over urban area but not as significant as that for non-TC cases.

Global warming's impact on mean rainfall over zero AH and non-zero AH conditions are also similar with each other (see **Figure 3.21 c** and **d**). The whole d03 enhanced mean rainfall by ~ 0.2 mm hr^{-1} (~ 9 %). A significant enhancement (decrement) is registered over the coast (ocean) in d03. This is consistent with **Figure 3.8 f**, a dry anomaly was found over the South China Sea in the GFDL-ESM2M. However, this anomaly was found based on less than 20 TC cases across two different climates, and the effect may sensitive to the selection of cases.

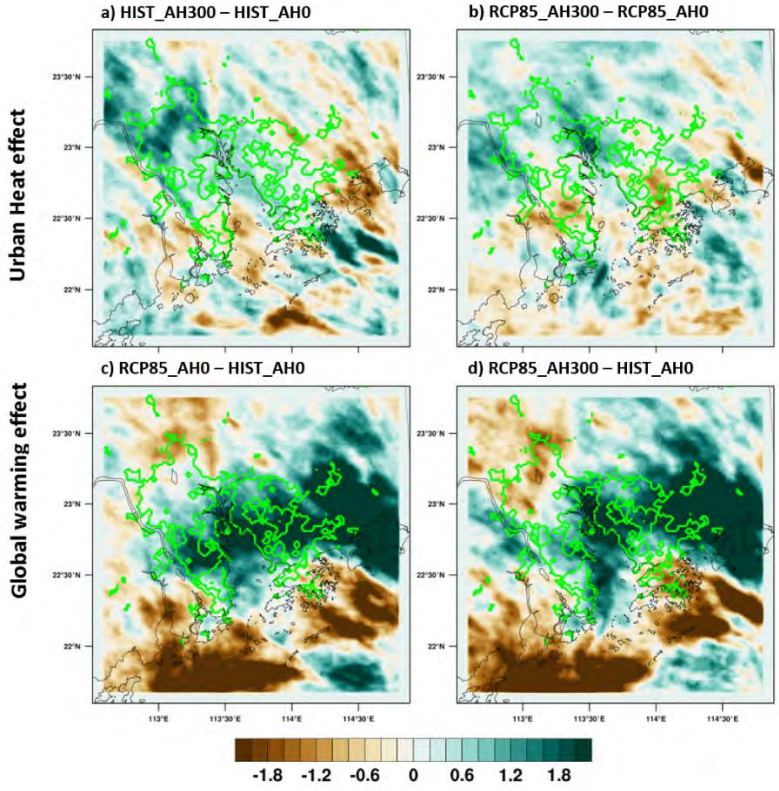

Figure 3.21 *Same as* ***Figure 3.9*** *with TC extreme cases.*

3.5.3. Impacts on rainfall characteristics

The hourly rainfall characteristics for TC-related extreme rainfall cases are further investigated. **Figure 3.22** displays the rainfall PDFs changes due to AH and global warming. The AH effect on the rainfall PDF based on TC cases seems to be very different from non-TC cases considered in section **3.4.2**. In the historical run, light rain (< 20 mm hr^{-1}) probability is decreased and at the same time heavier rain rates (> 20 mm hr^{-1}) are increased in urban area (see **Figure 3.22 a**), while the non-urban area does not show a significant change in the rainfall PDF. However, in the RCP 8.5 run, both urban and non-urban area does not have a significant change. This is consistent with the previous result that the stronger enhancement of mean rainfall was found in the historical run due to the AH effect, in comparison with the RCP 8.5 projections. The significance of the changes of rainfall PDFs were further evaluated in next part.

Global warming's effects are similar for zero and non-zero AH condition (see **Figure 3.22 c** and **d**). In the non-urban locations, both urbanization scenarios show similar results that heavy rain (> 20 mm hr^{-1}) probability is enhanced while the urban area shows a stronger increment for rain rate > 10 mm hr^{-1}. The different response between urban and non-urban area is consistent with mean rainfall response, which the wet anomaly was found overlaying the urban area and the dry anomaly was found over the ocean.

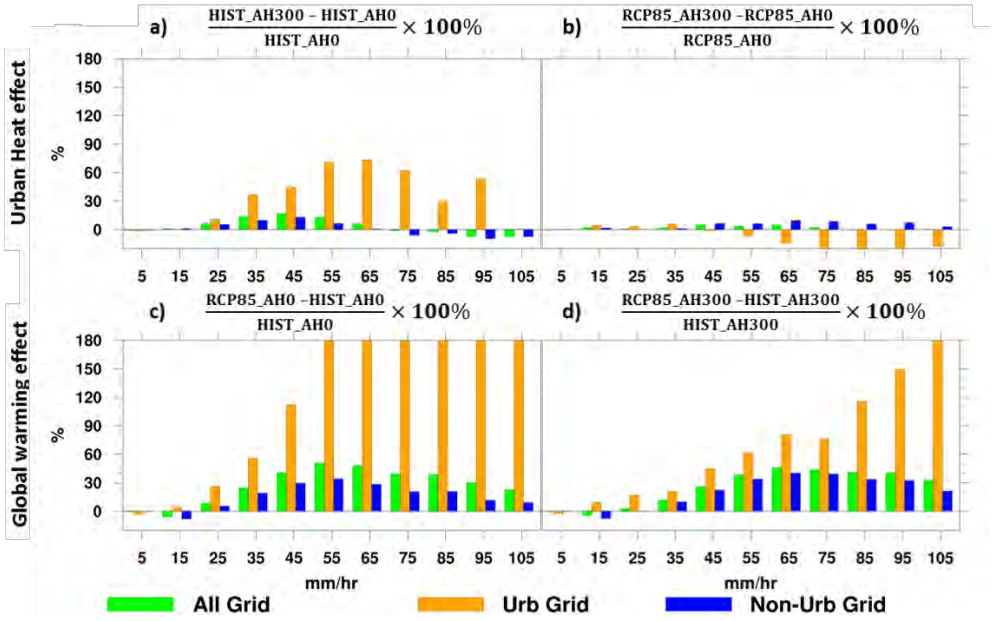

Figure 3.22 *Same as* ***Figure 3.11*** *with TC extreme cases*

The previous section shows significant shifts of rainfall PDFs for non-TC extreme cases, due to AH and global warming. However, for TC cases, AH's effects on rainfall PDFs do not give consistent results. **Figure 3.23** labelled the region that pass the 90 % confidence level in the KS test results. The AH effects in both climates also show that only a few areas have been shaded which indicate that the rainfall PDF do not change significantly over both urban and non-urban area (see **Figure 3.23 a** and **b**). In other words, the shift of rainfall PDF due to AH effect in historical climate may not be a significant result.

Global warming's effects are consistent in two urbanization scenarios. More than 50 % of the area in d03 have pass the 90 % confidence level of KS-test and mostly in the non-urban region (see **Figure 3.23 c** and **d**). Hence, the changes of rainfall PDFs in non-urban area are more significant than that over urban region.

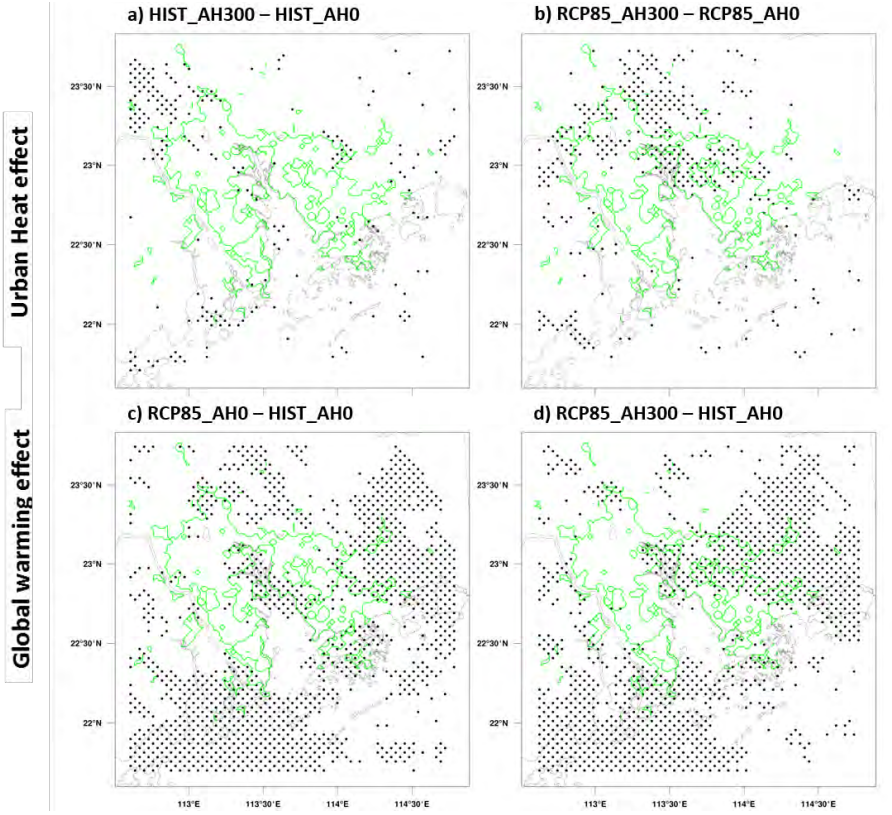

Figure 3.23 *Same as* ***Figure 3.12*** *with TC cases.*

3.5.4. Impacts on convective available potential energy and convective inhibition

The CAPE and CIN values have been evaluated for the TC cases, using the same method as in section **3.4.4**. The AH is seen to increase CAPE mainly in the urban area, for both historical and RCP 8.5 scenario (with stronger enhancement in the latter). On the other hand, global warming tends to enhance CAPE in the whole d03, especially over the ocean (see **Figure 3.24**). Such changes in CAPE are similar to that based on non-TC results (see **Figure 3.16**).

The AH effect leads to decrease in CIN over urban but increase in non-urban area (see **Figure 3.25**); again this is similar to the non-TC results (see **Figure 3.18**). In addition, there is less CIN decrement over urban area in the historical climate. On the other hand, CIN is enhanced by global warming effect. This is likely due to the fact that there is stronger warming in the mid-to-upper troposphere, which stabilizes the atmosphere and increases CIN.

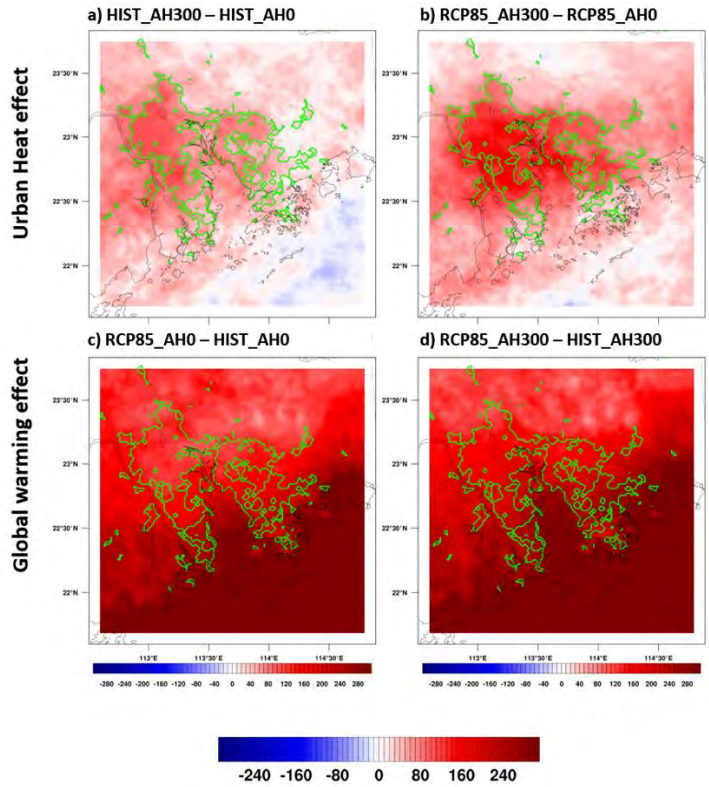

Figure 3.24 *Same as* ***Figure 3.16*** *plotting with the CAPE changes with TC cases. Units: J kg^{-1}.*

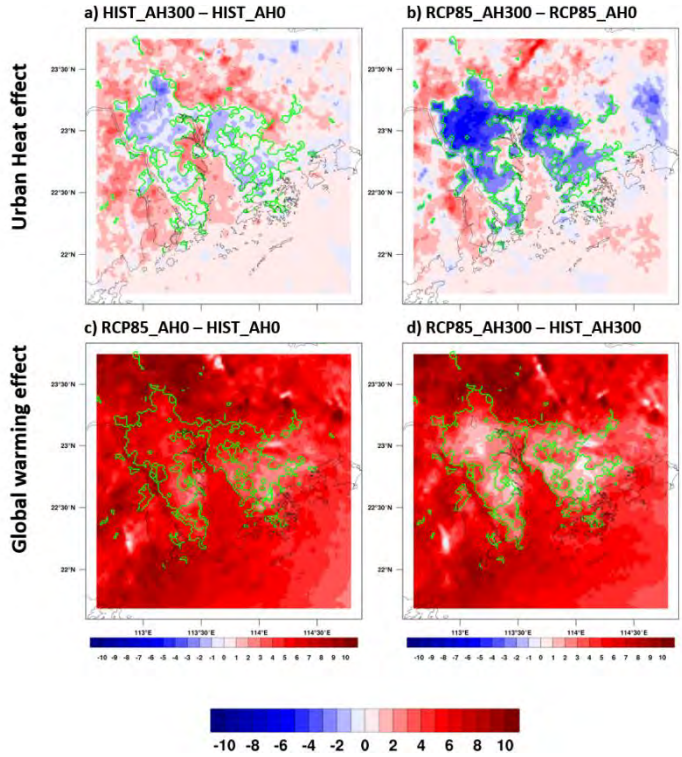

Figure 3.25 *Same as* ***Figure 3.18*** *plotting with the CIN changes with TC cases. Units: J kg^{-1}.*

Finally, we have also examined the time evolution of CAPE during the course of non-TC and TC related extreme rain events. **Figure 3.26** shows the time series of CAPE over urban grids of TC cases and non-TC cases in different experiments. CAPE values were spatially averaged over urban grids, with hour 0 denoting timing of simulated rainfall peak. For all non-TC cases (dotted lines), CAPE are seen to be decreasing before the peak in all experiments. For TC cases (solid lines), the decreasing rend in CAPE is absent. This suggests that for non-TC related heavy rain cases, CAPE over the PRD is 'consumed' as the local convection develops. Therefore, the enhanced surface temperature with CAPE due to AH may induce stronger precipitation. On the other hand, the development of convection obviously involved different physical processes for TC-related cases. This is probably the reason why TC-induced heavy rainfall is not sensitive to any local temperature enhancement, and hence the value of AH due to urban influence in the region.

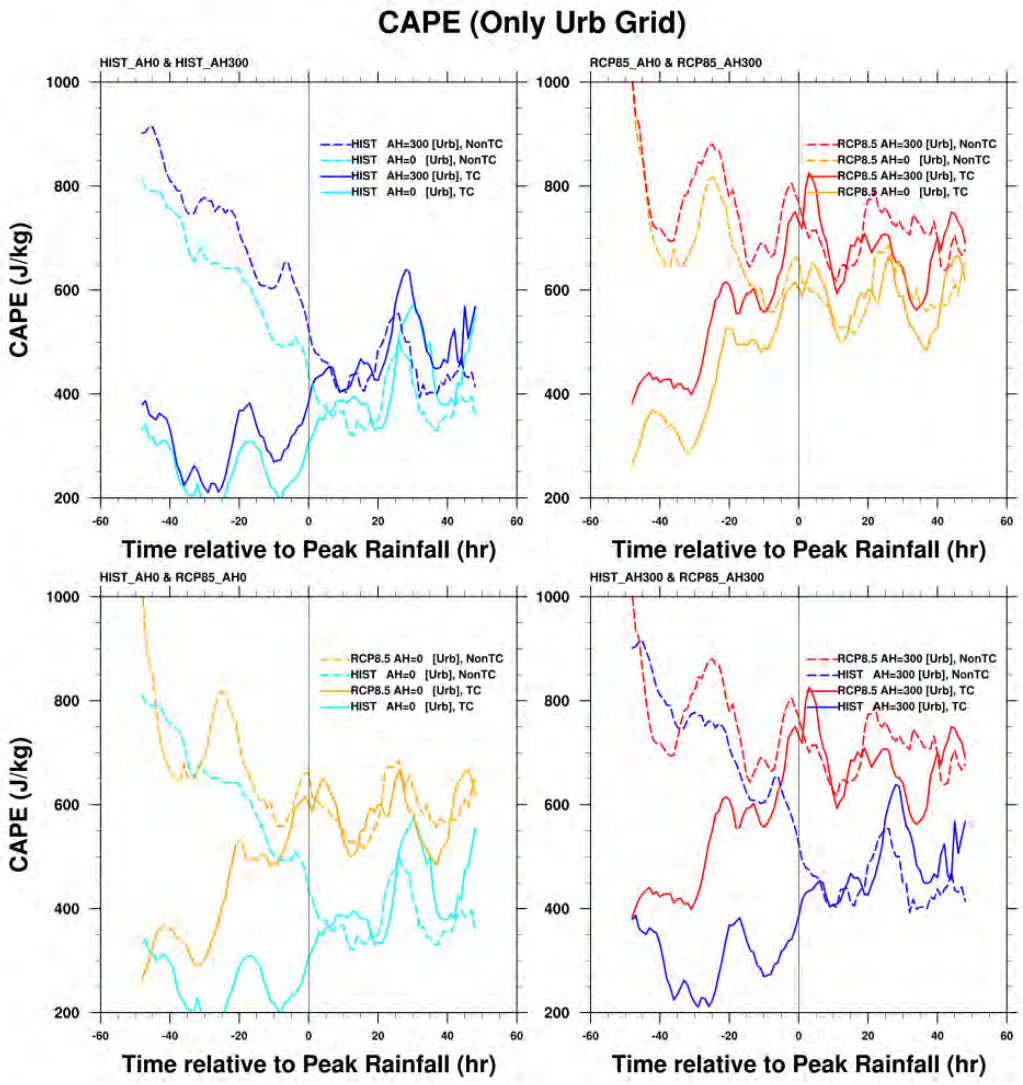

Figure 3.26 *CAPE times series for all experiments in TC cases (solid lines) and non-TC cases (dotted lines). The values were calculated plot the with the spatially averaged CAPE value over urban grids. 0 hr represented the hour simulated peak rainfall occurred.*

3.5.5. Impact of AH on circulation above urban area

To further investigate the effect of AH on the TC cases, similar vertical cross sections were plotted in **Figure 3.27** using the identical method that used in **Figure 3.19**. First of all, the near-surface warming zone have been found just above the city reaching ~ 1km high, which is similar with the non-TC results. The enhanced near-surface temperature produces more CAPE over urban area (see **Figure 3.24**) and hence stronger upward motion has been found over the urban area. However, the enhanced upward motion is not as strong as the non-TC cases. This is because the TC systems do not consume local CAPE for triggering intense rainfall. Also, enhanced CIN was found in the TC cases which tends to inhibit enhancement of upward motion due to AH effect.

Furthermore, the local circulation created by AH in TC cases seems to have smaller spatial scale compared with non-TC cases, in which the anomalous downward motion are found in between urban and sub-urban regions instead of having strong enhanced downward motion at the urban region periphery (see **Figure 3.19**). According to Lu et al., 1997, stronger ventilation environment will weaken the UHI effect. The averaged downscaled TC cases give a mean wind speed of 9 ms^{-1}, which shows a stronger ventilation compare with non-TC systems with average wind speed of ~ 6 ms^{-1}. This might be the reason that UHI-induced local circulation in TC cases are comparatively weaker.

The change of precipitation and local circulation might also be due to changes of TC landfall locations. We have tried to examine TC tracks by tracking these systems based on the local maxima (minima) of 850 hPa vorticity (sea level pressure or SLP) in the domain d03. However, when a TC approaches land, the SLP can become noisy and the TC track fluctuates very much. Furthermore, the d03 domain is too small to contain a significant portion of a typical TC track. Therefore, how AH might affect TC tracks and landfall positions is still inconclusive based on simulations done in this study.

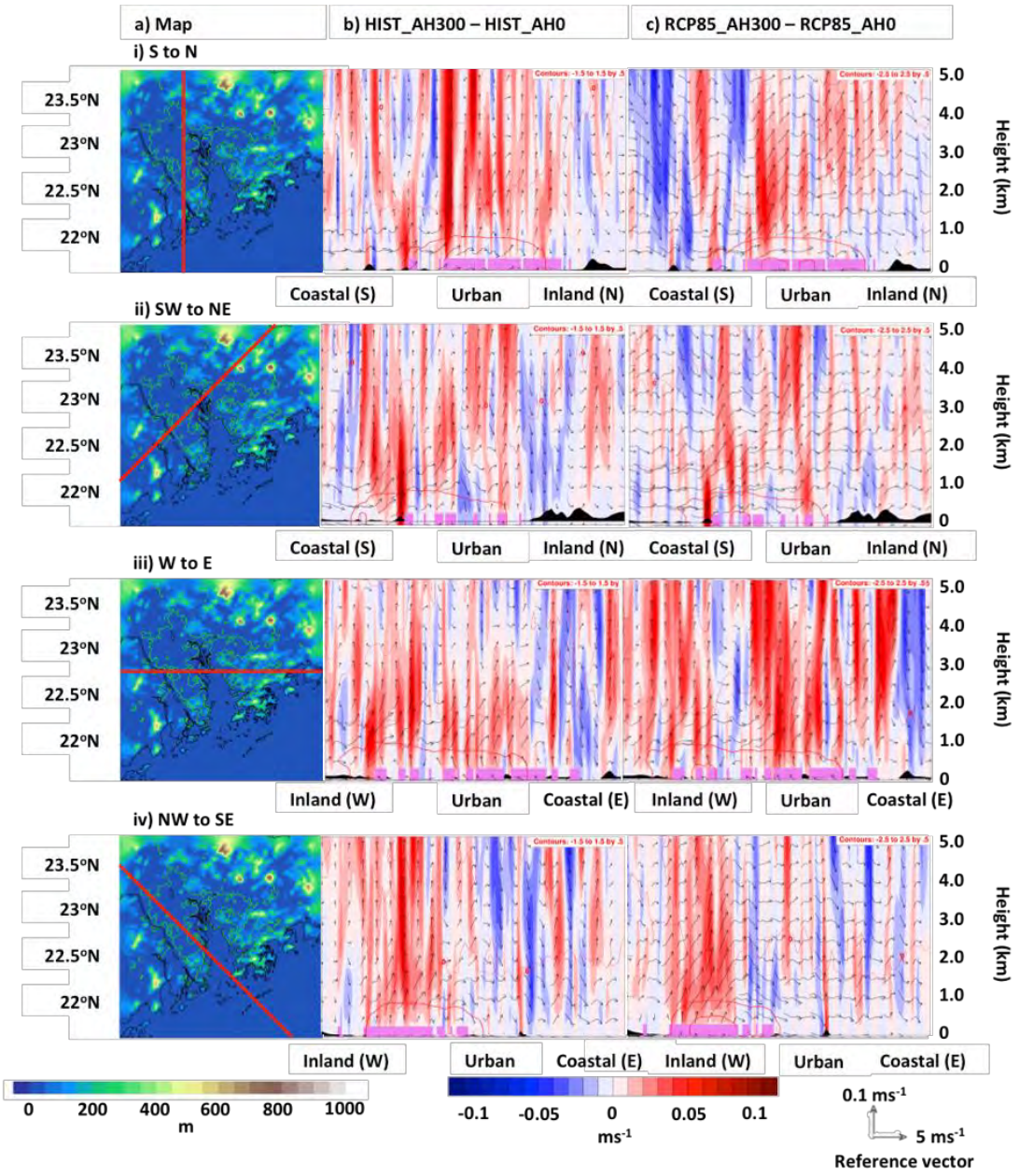

Figure 3.27 *Same as* ***Figure 3.19*** *with TC extreme cases*

3.6. Limitations and future investigation

In this study, extreme rainfall cases were identified by averaging 16 grids of a coarse spatial resolution (2º x 2.5º) GCM, GFDL-ESM2M. The region covers quite a large area; it is possible that heavy rain centres of some identified extreme rainfall cases may not be occurring over PRD, leading to underestimation of extreme rainfall condition in the area. Hence, AH effect on extreme rainfall events may not be that prominent. In future, to improve the case selection method, higher spatial resolution GCM can be used. At the same time, extreme rainfall from simulations has been compared with the satellite observation data TRMM-3B42 and underestimation of precipitation over southern China from GFDL-ESM2M was found. Therefore, the extreme rainfall events may milder compared with reality.

Secondly, only 12 (17) TC cases were simulated in historical (RCP 8.5) run, which is about half of the sample size of non-TC cases. Results given by TC cases might not be as robust as the non-TC simulations. On the other hand, there may not be a fair comparison between AH and global warming's effect. In our modelling framework, the AH effect was examined based on downscaling of the same set of synoptic systems; for assessing global warming's impact, different sets of weather systems (from the historical climate and future projections taken from GFDL-ESM2M) were considered. To improve the robustness of our results, more cases can be considered (for instance by relaxing the rain rate threshold to R95p).

The SLUCM parameters used in this study were based on conditions relevant to Hong Kong. Over the whole PRD region, it is likely that buildings may not be as compact as those in Hong Kong, meaning that AH is not uniformly distributed over the whole domain. Thus, the SLUCM parameters used can be regarded as a possible future scenario in which PRD is extremely urbanized. Furthermore, model default values for some UCM parameters are used, which might not be appropriate for the whole PRD region. For better characterization of the urban environment, the World Urban Database and Access Portal Tools (WUDAPT) data should be referenced. WUDAPT has mapped the world urban centres and classified their land areas into different kinds of urban land use based on building heights and compactness, thermal admittance of building materials and permeability of land surface etc. More accurate UCM parameters can be retrieved from this dataset.

The impact of urbanization on local/regional meteorology is not only mediated by anthropogenic heat. Other factors such as aerosols released and urban morphology can also play important roles. Over the PRD megacity, air pollution is a serious problem, and understanding the aerosols' impact on extreme events is especially important. Some studies have shown that aerosols can provide extra cloud condensation nuclei which produce smaller cloud droplets and hence suppress the intense rainfall. In future, simulation tools such as WRF-Chem that can properly capture various physical and chemical processes should be considered for investigating aerosols' effect on precipitation characteristics over PRD region. The urban morphology effects might also create turbulence and provide extra lifting such that convection can occure more easily.

4. Summary

This study examined the AH and global warming effects on extreme rainfall over the PRD region based on dynamically downscaling GFDL-ESM2M outputs using the WRF meso-scale model coupled with SLUCM. About 25 extreme non-TC and 15 TC-related extreme rainfall identified in the GFDL model were considered. For non-TC cases, AH released in the urban area lead to robust raise in surface temperature. This enhances CAPE and reduces CIN in the urban area which leads to more unstable atmosphere at the urban centre. Therefore, stronger convection takes place over the city, with more intense rainfall. There is an increase in the probability of heavy rainfall (> 10 mm hr^{-1}) in urban locations. The accumulated rainfall over these casses in the urban area is also enhanced. AH released in the urban area also induces an updraft anomaly above the city, consistent with stronger convection and heavier rainfall extreme over the urban locations.

The global warming effect impacts on wider region, with inrcreased surface temperature and values of CAPE, which increases the probability of both urban and non-urban heavy rainfall (> 20 mm hr^{-1}) for non-TC cases. However, the increment of probability of heavy non-urban rainfall is less than that over the urban area. This may be due to the fact that there is a dry anomaly overlaying the coastal area of southern China when comparing the RCP 8.5 with the historical run from the GFDL-ESM2M.

For TC cases, results are not as robust as the non-TC cases. The AH effects on surface temperature and CAPE are similar to the non-TC cases. Although the mean rainfall shows stronger enhancement in urban region, the pattern is different from the non-TC cases. The urban rainfall PDFs changes due to AH effect is also not as significant as the non-TC cases. This may due to the limited number of cases simulated. Furthermore, the rainfall mechanisms are different for non-TC and TC systems; for non-TC systems the local CAPE is consumed to produce convective rains, but for TC systems the local CAPE value does not decrease when convective rain occurs. Global warming effects show consistent results for zero AH and non-zero AH scenarios with significant enhancement of intense rainfall.

5. Bibliography

Ali, Haider, &Mishra, Vimal. (2017). Contrasting response of rainfall extremes to increase in surface air and dewpoint temperatures at urban locations in India. *Scientific Reports*, *7*(1), 1228. https://doi.org/10.1038/s41598-017-01306-1

Allen, L., Lindberg, F., &Grimmond, C. S. B. (2011). Global to city scale urban anthropogenic heat flux: Model and variability. *International Journal of Climatology*, *31*(13), 1990–2005. https://doi.org/10.1002/joc.2210

Arnfield, A. John. (2003). Two decades of urban climate research: A review of turbulence, exchanges of energy and water, and the urban heat island. *International Journal of Climatology*, *23*(1), 1–26. https://doi.org/10.1002/joc.859

Bornstein, Robert D. (1968). Observations of the Urban Heat Island Effect in New York City. *Journal of Applied Meteorology*. https://doi.org/10.1175/1520-0450(1968)007<0575:OOTUHI>2.0.CO;2

Bornstein, Robert, &Lin, Qinglu. (2000). Urban Heat İslands And summertime Convective Thunderstorms İn Atlanta: Three Case Studies. *Atmospheric Environment*, *34*, 507*516.

Bougeault, P., &Lacarrere, P. (1989). Parameterization of Orography-Induced Turbulence in a Mesobeta--Scale Model. *Monthly Weather Review*. https://doi.org/10.1175/1520-0493(1989)117<1872:POOITI>2.0.CO;2

Brown, Casey, Greene, Arthur, Block, Paul, &Giannini, Alessandra. (2008). *IRI Technical Report 08-05: IRI Downscaling Report Review of downscaling methodologies for Africa climate applications*.

Carlson, Toby N., Dodd, Joseph K., Benjamin, Stanley G., &Cooper, James N. (1981). Satellite Estimation of the Surface Energy Balance, Moisture Availability and Thermal Inertia. *Journal of Applied Meteorology*. https://doi.org/10.1175/1520-0450(1981)020<0067:SEOTSE>2.0.CO;2

Chan, L. Y., &Kwok, W. S. (2000). Vertical dispersion of suspended particulates in urban area of Hong Kong. *Atmospheric Environment*, *34*(26), 4403–4412. https://doi.org/10.1016/S1352-2310(00)00181-3

Changnon, Stanley a., &Karl, Thomas R. (2003). Temporal and Spatial Variations of Freezing Rain in the Contiguous United States: 1948–2000. *Journal of Applied Meteorology*, *42*(9), 1302–1315. https://doi.org/10.1175/1520-0450(2003)042<1302:TASVOF>2.0.CO;2

Chen, Fei, Kusaka, Hiroyuki, Bornstein, Robert, Ching, Jason, Grimmond, C. S. B., Grossman-Clarke, Susanne, Loridan, Thomas, Manning, Kevin W., Martilli, Alberto, Miao, Shiguang, Sailor, David, Salamanca, Francisco P., Taha, Haider, Tewari, Mukul, Wang, Xuemei, Wyszogrodzki, Andrzej A., &Zhang, Chaolin. (2011). The integrated WRF/urban modelling system: Development, evaluation, and applications to urban environmental problems. *International Journal of Climatology*, *31*(2), 273–288. https://doi.org/10.1002/joc.2158

Chen, HuoPo P. (2013). Projected change in extreme rainfall events in China by the end of the 21st century using CMIP5 models. *Chinese Science Bulletin*, *58*(12), 1462–1472. https://doi.org/10.1007/s11434-012-5612-2

Chou, Chia, Chen, Chao An, Tan, Pei Hua, &Chen, Kuan Ting. (2012). Mechanisms for global warming impacts on precipitation frequency and intensity. *Journal of Climate*, *25*(9), 3291–3306. https://doi.org/10.1175/JCLI-D-11-00239.1

Coceal, O., &Belcher, S. E. (2004). A canopy model of mean winds through urban areas. *Quarterly Journal of the Royal Meteorological Society*, *130*(599 PART B), 1349–1372. https://doi.org/10.1256/qj.03.40

Collier, C. G. (2006). The impact of urban areas on weather. *Quarterly Journal of the Royal Meteorological Society*. https://doi.org/10.1256/qj.05.199

Dee, D. P., Uppala, S. M., Simmons, A. J., Berrisford, P., Poli, P., Kobayashi, S., Andrae, U., Balmaseda, M. A., Balsamo, G., Bauer, P., Bechtold, P., Beljaars, A. C. M., van deBerg, L., Bidlot, J., Bormann, N., Delsol, C., Dragani, R., Fuentes, M., Geer, A. J., Haimberger, L., Healy, S. B., Hersbach, H., Hólm, E.V., Isaksen, L., Kållberg, P., Köhler, M., Matricardi, M., Mcnally, A. P., Monge-Sanz, B. M., Morcrette, J. J., Park, B. K., Peubey, C., deRosnay, P., Tavolato, C., Thépaut, J. N., &Vitart, F. (2011). The ERA-Interim reanalysis: Configuration and performance of the data assimilation system. *Quarterly Journal of the Royal Meteorological Society*, *137*(656), 553–597. https://doi.org/10.1002/qj.828

Dou, Jingjing, Wang, Yingchun, Bornstein, Robert, &Miao, Shiguang. (2015). Observed spatial characteristics of Beijing urban climate impacts on summer thunderstorms. *Journal of Applied Meteorology and Climatology*, *54*(1), 94–105. https://doi.org/10.1175/JAMC-D-13-0355.1

Du, Shiqiang, Shi, Peijun, &Rompaey, Anton. (2013). The Relationship between Urban Sprawl and Farmland Displacement in the Pearl River Delta, China. *Land*, *3*(1), 34–51. https://doi.org/10.3390/land3010034

Dudhia, Jimy. (1989). Numerical Study of Convection Observed during the Winter Monsoon Experiment Using a Mesoscale Two-Dimensional Model. *Journal of the Atmospheric Sciences*. https://doi.org/10.1175/1520-0469(1989)046<3077:NSOCOD>2.0.CO;2

Dunne, John P., John, Jasmin G., Adcroft, Alistair J., Griffies, Stephen M., Hallberg, Robert W., Shevliakova, Elena, Stouffer, Ronald J., Cooke, William, Dunne, Krista A., Harrison, Matthew J., Krasting, John P., Malyshev, Sergey L., Milly, P. C. D., Phillips, Peter J., Sentman, Lori T., Samuels, Bonita L., Spelman, Michael J., Winton, Michael, Wittenberg, Andrew T., &Zadeh, Niki. (2012). GFDL's ESM2 global coupled climate-carbon earth system models. Part I: Carbon system formulation and baseline simulation characteristics. *Journal of Climate*, *25*(19), 6646–6665. https://doi.org/10.1175/jcli-d-11-00560.1

Dunne, John P., John, Jasmin G., Shevliakova, Selena, Stouffer, Ronald J., Krasting, John P., Malyshev, Sergey L., Milly, P. C. D., Sentman, Lori T., Adcroft, Alistair J., Cooke, William, Dunne, Krista A., Griffies, Stephen M., Hallberg, Robert W., Harrison, Matthew J., Levy, Hiram, Wittenberg, Andrew T., Phillips, Peter J., &Zadeh, Niki. (2013). GFDL's ESM2 global coupled climate-carbon earth system models. Part II: Carbon system formulation and baseline simulation characteristics. *Journal of Climate*, *26*(7), 2247–2267. https://doi.org/10.1175/JCLI-D-12-00150.1

Fisher, Bernard, Kukkonen, J., Piringer, M., Rotach, M. W., &Schatzmann, M. (2006). Meteorology applied to urban air pollution problems: Concepts from COST 715. *Atmospheric Chemistry and Physics*, *6*(2), 555–564. https://doi.org/10.5194/acp-6-555-2006

Gaspar, Philippe, Andre, Jean-Claude, &Lefevre, Jean-Michel. (1990). The determination of the latent and sensible heat fluxes ate the sea surface viewed as an inverse problem. *Journal of Geophysical Research*, *95*(C9), 16169–16178.

Heywood, G. S. P. (1953). *Surface pressure-patterns & weather around the year in Hong Kong, Technical Memoirs 6*. Hong Kong.

Holst, Christopher Claus, Tam, Chi Yung, &Chan, Johnny C. L. (2016). Sensitivity of urban rainfall to anthropogenic heat flux: A numerical experiment. *Geophysical Research Letters*, *43*(5), 2240–2248. https://doi.org/10.1002/2015GL067628

Hong, S. Y., &J. Lim, J. O. (2006). The WRF single-moment 6-class microphysics scheme (WSM6). *Journal of the Korean Meteorological Society*, *42*, 129–151.

Hope, Tisdale. (1942). The Process of Urbanization. *Social Forces*, *20*(3), 311–316. https://doi.org/10.2307/3005615

Huff, F. A., &Changnon, S. A. (1973). Precipitation modillcallon by major urban areas. *Bulletin of the American Meteorological Society*, *54*(12), 1220–1232. https://doi.org/10.1175/1520-0477(1973)054<1220:pmbmua>2.0.co;2

Iacono, Michael J., Delamere, Jennifer S., Mlawer, Eli J., Shephard, Mark W., Clough, Shepard A., &Collins, William D. (2008). Radiative forcing by long-lived greenhouse gases: Calculations with the AER radiative transfer models. *Journal of Geophysical Research Atmospheres*. https://doi.org/10.1029/2008JD009944

Ichinose, Toshiaki, Shimodozono, Kazuhiro, &Hanaki, Keisuke. (1999). Impact of anthropogenic heat on urban climate in Tokyo. *Atmospheric Environment*, *33*(24–25), 3897–3909. https://doi.org/10.1016/S1352-2310(99)00132-6

Janjić, Zaviša I. (1994). The Step-Mountain Eta Coordinate Model: Further Developments of the Convection, Viscous Sublayer, and Turbulence Closure Schemes. *Monthly Weather Review*. https://doi.org/10.1175/1520-0493(1994)122<0927:TSMECM>2.0.CO;2

Jin, Menglin, Li, Yu, &Su, Debin. (2015). Urban-Induced Mechanisms for an Extreme Rainfall Event in Beijing China: A Satellite Perspective. *Climate*, *3*(1), 193–209. https://doi.org/10.3390/cli3010193

Kunz, M., Sander, J., &Kottmeier, Ch. (2009). Recent trends of thunderstorm and hailstorm frequency and their relation to atmospheric characteristics in southwest Germany. *International Journal of Climatology*, *29*(15), 2283–2297. https://doi.org/10.1002/joc.1865

Kusaka, Hiroyuki, &Kimura, Fujio. (2004). Thermal Effects of Urban Canyon Structure on the Nocturnal Heat Island: Numerical Experiment Using a Mesoscale Model Coupled with an Urban Canopy Model. *Journal of Applied Meteorology*, *43*(12), 1899–1910. https://doi.org/10.1175/JAM2169.1

Kusaka, Hiroyuki, Kondo, Hiroaki, Kikegawa, Yokihiro, &Kimura, Fujio. (2001). A simple single-layer urban canopy model for atmospheric models: Comparison with multi-layer and slab models. *Boundary-Layer Meteorology*. https://doi.org/10.1023/A:1019207923078

Kusaka, Hiroyuki, Nawata, Keiko, Suzuki-Parker, Asuka, Takane, Yuya, &Furuhashi, Nana. (2014). Mechanism of precipitation increase with urbanization in Tokyo as revealed by ensemble climate simulations. *Journal of Applied Meteorology and Climatology*, *53*(4), 824–839. https://doi.org/10.1175/JAMC-D-13-065.1

Lei, Zhang, &Hanqing, S. H. I. (2017). An evaluation of new satellite-derived latent and sensible heat fluxes with moored buoy data , OAFlux and NCEP2 reanalysis products, *36*(9), 27–38. https://doi.org/10.1007/s13131-017-1108-x

Lenderink, G., Mok, H. Y., Lee, T. C., &VanOldenborgh, G. J. (2011). Scaling and trends of hourly precipitation extremes in two different climate zones - Hong

Kong and the Netherlands. *Hydrology and Earth System Sciences*, *15*(9), 3033–3041. https://doi.org/10.5194/hess-15-3033-2011

Li, Jianping, Wu, Zhiwei, Jiang, Zhihong, &He, Jinhai. (2010). Can global warming strengthen the East Asian summer monsoon? *Journal of Climate*, *23*(24), 6696–6705. https://doi.org/10.1175/2010JCLI3434.1

Liu, Run, Liu, Shaw Chen, Cicerone, Ralph J., Shiu, CheinJung, Li, Jun, Wang, Jingli, &Zhang, Yuanhang. (2015). Trends of Extreme Precipitation in Eastern China and Their Possible Causes. *Advances in Atmospheric Sciences*, *32*(October), 1447–1448. https://doi.org/10.1007/s00376-015-5002-1.1.

Lo, Jeff Chun Fung, Yang, Zong Liang, &Pielke, Roger A. (2008). Assessment of three dynamical climate downscaling methods using the Weather Research and Forecasting (WRF) model. *Journal of Geophysical Research Atmospheres*, *113*(9). https://doi.org/10.1029/2007JDO09216

Lu, Jie, Arya, S. Pal, Snyder, William H., &Lawson, Robert E. (1997). A Laboratory Study of the Urban Heat Island in a Calm and Stably Stratified Environment. Part I: Temperature Field. *Journal of Applied Meteorology*, *36*(10), 1377–1391. https://doi.org/10.1175/1520-0450(1997)036<1377:ALSOTU>2.0.CO;2

Makar, P. A., Gravel, S., Chirkov, V., Strawbridge, K. B., Froude, F., Arnold, J., &Brook, J. (2006). Heat flux, urban properties, and regional weather. *Atmospheric Environment*, *40*(15), 2750–2766. https://doi.org/10.1016/j.atmosenv.2005.11.061

Maltese, Antonino, Awada, Hassan, Capodici, Fulvio, Ciraolo, Giuseppe, Loggia, GoffredoLa, &Rallo, Giovanni. (2018). On the use of the eddy covariance latent heat flux and sap flow transpiration for the validation of a surface energy balance model. *Remote Sensing*, *10*(2), 1–17. https://doi.org/10.3390/rs10020195

McSweeney, C. F., Jones, R. G., Lee, R. W., &Rowell, D. P. (2015). Selecting CMIP5 GCMs for downscaling over multiple regions. *Climate Dynamics*, *44*(11–12), 3237–3260. https://doi.org/10.1007/s00382-014-2418-8

Monin, A. S., &Obukhov, A. M. (1954). Basic laws of turbulent mixing in the surface layer of the atmosphere. *Inst. Contract Number*, *24*(19604), 163–187.

Moss, Richard H., Edmonds, Jae A., Hibbard, Kathy A., Manning, Martin R., Rose, Steven K., VanVuuren, Detlef P., Carter, Timothy R., Emori, Seita, Kainuma, Mikiko, Kram, Tom, Meehl, Gerald A., Mitchell, John F. B., Nakicenovic, Nebojsa, Riahi, Keywan, Smith, Steven J., Stouffer, Ronald J., Thomson, Allison M., Weyant, John P., &Wilbanks, Thomas J. (2010). The next generation of scenarios for climate change research and assessment. *Nature*, *463*(7282), 747–756. https://doi.org/10.1038/nature08823

Nielsen, L. B., Prahm, L. P., Berkowicz, R., &Conradsen, K. (1981). Net incoming radiation estimated from hourly global radiation and/or cloud observations. *Journal of Climatology*, *1*(3), 255–272. https://doi.org/10.1002/joc.3370010305

Nieuwolt, S. (1966). The urban microclimate of Singapore. *The Journal of Tropical Geography*, (22), 30–31.

Oke, T. R. (1973). City size and the urban heat island. *Atmospheric Environment Pergamon Pres*, *7*, 769–779. https://doi.org/10.1016/0004-6981(73)90140-6

Oke, T. R. (1976). The distinction between canopy and boundary layer urban heat islands. *Atmosphere*, *14*(July 2015), 268–277. https://doi.org/10.1080/00046973.1976.9648422

Oke, T. R. (1981). Canyon geometry and the nocturnal urban heat island: coparison of scale model and field observations. *J. Climatology*, *1*, 237–254.

Oke, T. R. (1988). The urban energy balance. *Progress in Physical Geography*, *12*(4), 471–508. https://doi.org/10.1177/030913338801200401

Onder, Serpil, &Dursun, Sukru. (2010). Global Climate Changes and Effects on Urban Climate of Urban Green Spaces. *International Journal of Thermal and Environmental Engineering*, *3*(1), 37–41. https://doi.org/10.5383/ijtee.03.01.006

Otte, T. L., &Gilliam, R. C. (2007). A Nudging Strategy for Mesobeta-Scale WRF Simulations Suitable for Retrospective Air Quality Modeling: Preliminary Results. In *NOAA Air Resources Laboratory, Research Triangle Park, NC (In partnership with U.S. EPA National Exposure Research Laboratory). 6th Annual CMAS Conference, Chapel Hill, NC.*

Pan H. L., &Wu W.-S. (1995). *Implementing a mass flux convection parameterization package for the nmc medium-range forecast model*. Retrieved from http://www2.mmm.ucar.edu/wrf/users/phys_refs/CU_PHYS/Old_SAS.pdf

Poelmans, Lien, &VanRompaey, Anton. (2009). Detecting and modelling spatial patterns of urban sprawl in highly fragmented areas: A case study in the Flanders-Brussels region. *Landscape and Urban Planning*, *93*(1), 10–19. https://doi.org/10.1016/j.landurbplan.2009.05.018

Qian, Weihong, Fu, Jiaolan, &Yan, Zhongwei. (2007). Decrease of light rain events in summer associated with a warming environment in China during 1961-2005. *Geophysical Research Letters*, *34*(11), 1–5. https://doi.org/10.1029/2007GL029631

Rosenfeld, Daniel, Lohmann, Ulrike, Raga, Graciela B., O'Dowd, Colin D., Kulmala, Markku, Fuzzi, Sandro, Reissell, Anni, &Andreae, Meinrat O. (2008). Flood or drought: How do aerosols affect precipitation? *Science*, *321*(5894), 1309–1313. https://doi.org/10.1126/science.1160606

Rozoff, Christopher M., Cotton, William R., &Adegoke, Jimmy O. (2003). Simulation of St . Louis , Missouri , Land Use Impacts on Thunderstorms. *Journal of Applied Meteorology and Climatology*, *42*(6), 716–738. https://doi.org/10.1175/1520-0450(2003)042<0716:SOSLML>2.0.CO;2

Shepherd, J. M. (2005). A review of current investigations of urban-inudced rainfall and recommendations for the future. *Earth Interactions*, *9*(12). https://doi.org/10.1175/EI156.1

Sisterson, Douglas L., &Dirks, Richard A. (2015). The urban moisture climate. *Proceedings of the Conference on Metropolitan Physical Environment.*, *Gen. Tech.*(August), 26–35.

Skamarock, W. C., Klemp, J. B., Dudhi, J., Gill, D. O., Barker, D. M., Duda, M. G., Huang, X. Y., Wang, W., &Powers, J. G. (2008). A Description of the Advanced Research WRF Version 3. *Technical Report*, (June), 113. https://doi.org/10.5065/D6DZ069T

Taha, Haider. (1997). Urban climates and heat islands: albedo, evapotranspiration, and anthropogenic heat. *Energy and Buildings*, *25*(2), 99–103. https://doi.org/10.1016/S0378-7788(96)00999-1

Taylor, Karl E. (2005). Taylor Diagram Primer. *Working Paper*, (January), 1–4. https://doi.org/10.1029/2000JD900719

Trzaska, S., &Schnarr, E. (2014). A review of downscaling methods for climate change projections. *United States Agency for International Development by Tetra Tech ARD*, (September), 1–42.

Ueda, Hiroaki, Iwai, Ayaka, Kuwako, Ken, &Hori, Masatake E. (2006). Impact of anthropogenic forcing on the Asian summer monsoon as simulated by eight

GCMs. *Geophysical Research Letters*, *33*(6), 20–23. https://doi.org/10.1029/2005GL025336

vonStorch, Hans, Langenberg, Heike, &Feser, Frauke. (2000). A Spectral Nudging Technique for Dynamical Downscaling Purposes. *Monthly Weather Review*, *128*(10), 3664–3673. https://doi.org/10.1175/1520-0493(2000)128<3664:ASNTFD>2.0.CO;2

Wilby, R. L., Troni, J., Tedd, L., Hewitson, B. C., Smith, D. M., &Sutton, R. T. (2009). A review of climate risk information for adaptation and development planning. *International Journal of Climatology*, *29*(9), 1193–1215.

Wong, Man Sing, Yang, Jinxin, Nichol, Janet, Weng, Qihao, Menenti, Massimo, &Chan, P. W. (2015). Modeling of Anthropogenic Heat Flux Using HJ-1B Chinese Small Satellite Image: A Study of Heterogeneous Urbanized Areas in Hong Kong. *IEEE Geoscience and Remote Sensing Letters*. https://doi.org/10.1109/LGRS.2015.2409111

Xie, Min, Liao, Jingbiao, Wang, Tijian, Zhu, Kuanguang, Zhuang, Bingliang, Han, Yong, Li, Mengmeng, &Li, Shu. (2016). Modeling of the anthropogenic heat flux and its effect on regional meteorology and air quality over the Yangtze River Delta region, China. *Atmospheric Chemistry and Physics*, *16*(10), 6071–6089. https://doi.org/10.5194/acp-16-6071-2016

Yan, Zhong Wei, Wang, Jun, Xia, Jiang Jiang, &Feng, Jin Ming. (2016). Review of recent studies of the climatic effects of urbanization in China. *Advances in Climate Change Research*, *7*(3), 154–168. https://doi.org/10.1016/j.accre.2016.09.003

Yang, Wangming, Chen, Bing, &Cui, Xuefeng. (2014). High-resolution mapping of anthropogenic heat in China from 1992 to 2010. *International Journal of Environmental Research and Public Health*, *11*(4), 4066–4077. https://doi.org/10.3390/ijerph110404066